NASA/TM—2014–216616

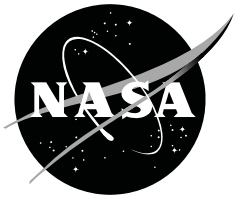

# Virtual Deformation Control of the X-56A Model with Simulated Fiber Optic Sensors

*Peter M. Suh and Alexander W. Chin*
*Dryden Flight Research Center, Edwards, California*

*Dimitri N. Mavris*
*Georgia Institute of Technology, Atlanta, Georgia*

**January 2014**

# NASA STI Program ... in Profile

Since its founding, NASA has been dedicated to the advancement of aeronautics and space science. The NASA scientific and technical information (STI) program plays a key part in helping NASA maintain this important role.

The NASA STI program operates under the auspices of the Agency Chief Information Officer. It collects, organizes, provides for archiving, and disseminates NASA's STI. The NASA STI program provides access to the NTRS Registered and its public interface, the NASA Technical Reports Server, thus providing one of the largest collections of aeronautical and space science STI in the world. Results are published in both non-NASA channels and by NASA in the NASA STI Report Series, which includes the following report types:

- TECHNICAL PUBLICATION. Reports of completed research or a major significant phase of research that present the results of NASA Programs and include extensive data or theoretical analysis. Includes compilations of significant scientific and technical data and information deemed to be of continuing reference value. NASA counterpart of peer-reviewed formal professional papers but has less stringent limitations on manuscript length and extent of graphic presentations.

- TECHNICAL MEMORANDUM. Scientific and technical findings that are preliminary or of specialized interest, e.g., quick release reports, working papers, and bibliographies that contain minimal annotation. Does not contain extensive analysis.

- CONTRACTOR REPORT. Scientific and technical findings by NASA-sponsored contractors and grantees.

- CONFERENCE PUBLICATION. Collected papers from scientific and technical conferences, symposia, seminars, or other meetings sponsored or co-sponsored by NASA.

- SPECIAL PUBLICATION. Scientific, technical, or historical information from NASA programs, projects, and missions, often concerned with subjects having substantial public interest.

- TECHNICAL TRANSLATION. English-language translations of foreign scientific and technical material pertinent to NASA's mission.

Specialized services also include organizing and publishing research results, distributing specialized research announcements and feeds, providing information desk and personal search support, and enabling data exchange services.

For more information about the NASA STI program, see the following:

- Access the NASA STI program home page at http://www.sti.nasa.gov

- E-mail your question to help@sti.nasa.gov

- Phone the NASA STI Information Desk at 757-864-9658

- Write to:
  NASA STI Information Desk
  Mail Stop 148
  NASA Langley Research Center
  Hampton, VA 23681-2199

NASA/TM—2014–216616

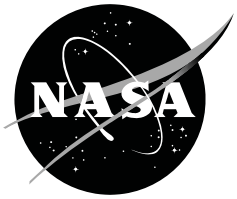

# Virtual Deformation Control of the X-56A Model with Simulated Fiber Optic Sensors

*Peter M. Suh and Alexander W. Chin*
*Dryden Flight Research Center, Edwards, California*

*Dimitri N. Mavris*
*Georgia Institute of Technology, Atlanta, Georgia*

National Aeronautics and
Space Administration

*Dryden Flight Research Center*
*Edwards, CA 93523-0273*

**January 2014**

## Acknowledgments

This research was funded by the NASA Aeronautics Research Mission Directorate Subsonic Fixed Wing Project and was approved by Steve Jacobson. Mr. Jacobson, the Dryden Controls Branch Chief; John Bosworth, the X-56A Chief Engineer; Jack Ryan, the X-56A Principal Investigator; Ryan Stillwater, the X-56A Controls Lead; Chan-gi Pak, the creator of the X-56A aeroservoelastic model; and the aeroservoelasticity expert Marty Brenner; have all been excellent advisors in the development of these results.

Available from:

NASA Center for AeroSpace Information
7115 Standard Drive
Hanover, MD 21076-1320
443-757-5802

# Abstract

A robust control law design methodology is presented to stabilize the X-56A model and command its wing shape. The X-56A was purposely designed to experience flutter modes in its flight envelope. The methodology introduces three phases: the controller design phase, the modal filter design phase, and the reference signal design phase. A mu-optimal controller is designed and made robust to speed and parameter variations. A conversion technique is presented for generating sensor strain modes from sensor deformation mode shapes. The sensor modes are utilized for modal filtering and simulating fiber optic sensors for feedback to the controller. To generate appropriate virtual deformation reference signals, rigid-body corrections are introduced to the deformation mode shapes. After successful completion of the phases, virtual deformation control is demonstrated. The wing is deformed and it is shown that angle-of-attack changes occur which could potentially be used to an advantage. The X-56A program must demonstrate active flutter suppression. It is shown that the virtual deformation controller can achieve active flutter suppression on the X-56A simulation model.


# Nomenclature

| | |
|---|---|
| $A$ | state matrix |
| AFS | active flutter suppression |
| AF | airframe |
| $AS$ | number of airframe states |
| AWBT | antisymmetric wing bending and torsion flutter mode |
| AW1B | antisymmetric wing first bending |
| AW1T | antisymmetric wing first torsion |
| $A_o$ | rational approximation matrix |
| $A_1$ | rational approximation matrix |
| $A_2$ | rational approximation matrix |
| $a$ | number of control surfaces |
| $a_\Delta$ | additive uncertainty signal |
| $B$ | control input matrix |
| BFF | body freedom flutter mode |
| BFL | body flap left |
| BFR | body flap right |
| $C$ | sensor output matrix |
| $cg$ | center of gravity |
| $D$ | direct feed-through matrix |
| DOF | degrees of freedom |
| $D_\omega$ | frequency weighting matrix |
| $d_{ref}$ | reference deformations |
| $d(x_C, y_C, z_C, t)$ | vector of deformations at positions $x_C$, $y_C$, $z_C$ at time $t$ |
| $E$ | rational approximation matrix of lag terms |
| FEM | finite element model |
| FOS | fiber optic sensors |
| $F_i$ | objective function for the $i^{th}$ mode |
| $f$ | number of aerodynamic lag states |
| freq | frequency |
| $G$ | plant |
| GAF | generalized aerodynamic force |
| $G_V$ | set of plants over a velocity range |

$G_{des}$ design plant
$g$ damping
I identity matrix
$i_\Delta$ input uncertainty signal
$\hat{\imath}$ imaginary number
$J$ generalized damping matrix
$K$ controller
$k_m$ stability margin
$L$ characteristic length
LFT linear fractional transformation
LWLE left-wing leading edge
LWTE left-wing trailing edge
$l_r$ sensor row index vector for reference deformations
$M$ generalized mass matrix
$M_\Delta$ matrix transfer function
$m$ number of modes in model
$m_r$ modal column index vector for reference modes
$N$ number of nodes in finite element model
NS nominal stability
NP nominal performance
$N_\Delta$ matrix transfer function
$n$ number of states
$n_r$ rigid body sensor noise
$n_s$ fiber optic sensor noise
$n_u$ input control noise
$O_s$ original sensor position before modal deformation
$O_s'$ original sensor position after modal deformation
$\overline{OP}$ line segment distance from point $O$ to point $P$
$\overline{O'P'}$ line segment distance from point $O'$ to point $P'$
$o$ number of measurements
$o_\Delta$ output uncertainty signal
P sensor location point
$P_g$ generalized plant
$P_+$ sensor position on the fore side of original sensor before modal deformation
$P_+'$ sensor position on the fore side of original sensor after modal deformation
$P_-$ sensor position on the aft side of original sensor before modal deformation
$P_-'$ sensor position on the aft side of original sensor after modal deformation
$Proj_{\vec{u}(\overrightarrow{O_sP_+})}\overrightarrow{O_s'P_+'}$ projection of directed segment $\overrightarrow{O_s'P_+'}$ on unit vector in the direction of $\overrightarrow{O_sP_+}$
$Proj_{\vec{u}(\overrightarrow{O_sP_-})}\overrightarrow{O_s'P_-'}$ projection of directed segment $\overrightarrow{O_s'P_-'}$ on unit vector in the direction of $\overrightarrow{O_sP_-}$
$Proj_{\vec{u}(\overrightarrow{OP})}\overrightarrow{O'P'}$ projection of directed segment $\overrightarrow{O'P'}$ on unit vector in the direction of $\overrightarrow{OP}$
$Q$ generalized aerodynamic force matrix
$\tilde{Q}(s)$ rational function approximation of the generalized aerodynamic forces
$q(t)$ vector of modal displacements at time $t$
$\dot{q}(t)$ vector of modal velocities at time $t$
$\ddot{q}(t)$ vector of modal accelerations at time $t$
$q_i(t)$ $i^{th}$ modal displacement defined at time $t$
$q_{ref}$ modal reference displacement command
$R$ diagonal matrix of lag roots

RP robust performance
RS robust stability
RWLE right-wing leading edge
RWTE right-wing leading edge
$(\cdot)_{ref}$ reference command of the argument
$S$ generalized stiffness matrix
SFOS simulated fiber optic sensors
$SP$ short-period mode
SWBT symmetric wing bending and torsion flutter mode
SW1B symmetric wing first bending
SW1T symmetric wing first torsion
$S_I$ input sensitivity matrix
$S_O$ output sensitivity matrix
$S_d$ strain-displacement transformation matrix
$s$ Laplace variable
$sim$ simulation
$s_m(x_C, y_C, z_C, t)$ strain at measurement locations at time $t$
$T(\cdot)$ right-hand-rotation matrix
$T_I$ input complementary sensitivity matrix
$T_O$ output complementary sensitivity matrix
$t$ time
$u$ control signal vector
$u(t)$ control input signal vector at time $t$
$\vec{u}(\cdot)$ unit vector
V-f frequency versus velocity
V-g damping versus velocity
$V_{des}$ design speed
$V_\infty$ free-stream velocity
$v$ error vector from reference input minus measurements
$W$ weighting
WF wing flap
WF1R wing flap first right
WF1L wing flap first left
WF2R wing flap second right
WF2L wing flap second left
WF3R wing flap third right
WF3L wing flap third left
WF4R wing flap fourth right
WF4L wing flap fourth left
$W_A$ matrix of proper additive weights
$W_I$ matrix of proper input weights
$W_O$ matrix of proper output weights
$W_S$ matrix of proper sensitivity weights
$W_T$ matrix of proper complementary sensitivity weights
$W_u$ matrix of proper control output weights
$w$ disturbance inputs
$X$ data matrix
$x(t)$ state vector at time $t$
$\dot{x}(t)$ state derivative vector at time $t$
$x_C$ Cartesian coordinate in the x-direction

| | |
|---|---|
| $x_{AF}$ | vector of airframe states |
| $x_{AF}^{ref}$ | reference airframe states |
| $x_{AF}(t)$ | vector of airframe states at time $t$ |
| $x_{act}(t)$ | vector of actuator displacements, velocities and accelerations at time $t$ |
| $x_{cg}$ | c.g. location of the aircraft in the $x_C$ direction |
| $x_e$ | vector of modal displacements |
| $x_l$ | uni-axial coordinate in a moving frame always in the direction of the SFOS layout |
| $x_{lag}(t)$ | vector of aero lag states at time $t$ |
| $x_o$ | initial state at time 0 |
| $x_e$ | modal displacements |
| $x_e(t)$ | vector of modal displacements at time $t$ |
| $x_{\dot{e}}(t)$ | vector of modal velocities at time $t$ |
| $x_u$ | un-deformed location of the aircraft nodes in the $x_C$ direction |
| $x_\phi^i$ | deformed location of aircraft nodes for the $i^{th}$ mode shape in $x_C$ |
| $\tilde{x}_e$ | estimated modal displacement states |
| $Y$ | rational approximation matrix of lag terms |
| $y$ | output sensor vector |
| $y(t)$ | output sensor vector at time $t$ |
| $y_C$ | Cartesian coordinate in the y-direction |
| $y_{cg}$ | c.g. location of the aircraft in the $y_C$ direction |
| $y_u$ | un-deformed location of the aircraft nodes in the $y_C$ direction |
| $y_\phi^i$ | deformed location of aircraft nodes for the $i^{th}$ mode shape in $y_C$ |
| $z$ | number of actuator states |
| $z_C$ | Cartesian coordinate in the z-direction |
| $z_{KS}$ | goal regulated $KS$ states |
| $z_S$ | goal regulated sensitivity states |
| $z_T$ | goal regulated complementary sensitivity states |
| $z_{cg}$ | c.g. location of the aircraft in the $z_C$ direction |
| $z_u$ | un-deformed location of the aircraft nodes in the $z_C$ direction |
| $z_\phi^i$ | deformed location of aircraft nodes for the $i^{th}$ mode shape in $z_C$ |
| $\alpha$ | angle of attack |
| $\beta$ | angle of sideslip |
| $\Delta$ | structured uncertainty |
| $\Delta_I$ | input uncertainty |
| $\delta V$ | change of velocity |
| $\delta\alpha$ | change of angle of attack |
| $\delta\theta$ | change in pitch angle |
| $\delta x_C$ | scalar global displacement in $x_C$ |
| $\delta x_{cm}$ | forward change of aircraft's center of mass from trim |
| $\delta y_C$ | scalar global displacement in $y_C$ |
| $\delta y_{cm}$ | side change of aircraft's center of mass from trim |
| $\delta z_C$ | scalar global displacement in $z_C$ |
| $\delta z_{cm}$ | heave change of the aircraft's center of mass from trim |
| $\delta\theta_C$ | scalar global angle about $y_C$ axis |
| $\delta\phi_C$ | scalar global angle about $x_C$ axis |
| $\delta\psi_C$ | scalar global angle about $z_C$ axis |
| $\delta LWLE$ | change in deformation at LWLE |
| $\delta LWTE$ | change in deformation at LWTE |

| | |
|---|---|
| $\delta RWLE$ | change in deformation at RWLE |
| $\delta RWTE$ | change in deformation at RWTE |
| $\delta SW1T$ | change in SW1T modal displacement |
| $\delta SW1B$ | change in SW1B modal displacement |
| $\delta WF1R$ | change in WF1R rotation |
| $\delta WF1L$ | change in WF1L rotation |
| $\delta WF2R$ | change in WF2R rotation |
| $\delta WF2L$ | change in WF2L rotation |
| $\delta WF3R$ | change in WF3R rotation |
| $\delta WF3L$ | change in WF3L rotation |
| $\delta WF4R$ | change in WF4R rotation |
| $\delta WF4L$ | change in WF4L rotation |
| $\varepsilon$ | measurement error |
| $\varepsilon_{xx}$ | axial strain |
| $\varepsilon_{xx}^{+}$ | axial strain measured on fore side of a sensor |
| $\varepsilon_{xx}^{-}$ | axial strain measured on aft side of a sensor |
| $\theta$ | pitch angle |
| $\mu$ | structured singular value |
| $\rho_{\infty}$ | free-stream density |
| $\bar{\sigma}$ | maximum singular value |
| $\Phi$ | deformation modal matrix, a collection of mode shapes, $\phi_m$ |
| $\phi$ | bank angle |
| $\phi_i$ | $i^{\text{th}}$ natural deformation mode shape |
| $\phi_i(x_C, y_C, z_C)$ | $i^{\text{th}}$ natural deformation mode shape defined over $x_C, y_C, z_C$ |
| $\Psi$ | strain mode matrix, a collection of strain mode shapes |
| $\Psi_{FOS}$ | strain matrix defined at the SFOS locations |
| $\psi$ | yaw angle |
| $\psi_i$ | $i^{th}$ strain mode |
| $\psi_m$ | $m^{th}$ strain mode |
| $\omega$ | frequency |
| $\frac{\partial u}{\partial x_l}$ | derivative in axial beam deformation in coordinate direction $x_l$ |
| $\mathcal{H}_{\infty}$ | Hardy space norm |

# Introduction

The NASA Aeronautics Research Mission Directorate (ARMD) is focusing on developing technology for dramatically reducing noise and emissions while improving performance for transport aircraft (ref. 1). New technology must support the decrease of aircraft fuel and energy consumption by 60 percent within a timeline of 15 years. One method of achieving this goal is to design new lightweight aircraft. The consequence of using a lighter structure with increased flexibility is that the structure is more likely to experience adverse aeroelastic effects such as flutter and divergence (ref. 2). Researchers suggest that flexible aircraft may be more susceptible than traditional aircraft to gusts and maneuver loading (ref. 3). Aircraft designed with lightweight flexible structures will require active control technology to be feasible alternatives to stiffer aircraft (ref. 4).

Research into active flutter suppression (AFS) technology on flexible aircraft is ongoing. The United States Air Force Research Laboratory (AFRL) Multi-utility Aeroelastic Demonstration (MAD) Program has developed the Multi Utility Technology Test-bed (MUTT), also known as the X-56A (Lockheed Martin, Bethesda, Maryland) (ref. 5). The X-56A is a flutter demonstrator designed for the sole purpose of testing various AFS solutions. Lockheed Martin is the prime contractor for design and development of

the vehicle. The X-56A stems from previous work between Lockheed Martin and the AFRL to design and develop high-altitude, subsonic, long-endurance autonomous aircraft (refs. 6 and 7).

The X-56A is a remotely-piloted aircraft with a stiff center body and flexible detachable wings. Due to the high flexibility of the wings, at certain speeds within the flight envelope the aircraft modes couple unfavorably, leading to three flutter instabilities. A control system must be developed with existing sensors and actuators to suppress the instabilities. Robust control of these flutter modes will demonstrate that lightweight structures can be implemented and flown safely. As part of its sensor array, the X-56A aircraft wings will be instrumented with fiber optic sensors (FOS) and fiber Bragg gratings (ref. 8). Fiber optic sensors fall into a class of distributed sensors and can measure strain at thousands of locations. A research objective in the X-56A program is to use these sensors in a feedback control system. This is the problem this report specifically addresses.

Active flutter suppression technology may be extended to not only suppress flutter modes, but to also control the shape of the aircraft. Research has been published which indicates that drag can be reduced due to structural deformation changes (ref. 9). The X-53 Active Aeroelastic Wing aircraft (The Boeing Company, Chicago, Illinois) warped its wing to achieve higher roll rates, improving its maneuverability (ref. 10). Research in shape control is ongoing. Smart technologies such as adaptive control surfaces (ref. 11), adaptive ribs (ref. 12), piezoelectric (ref. 13), and piezoceramic actuators (ref. 14) are under investigation. Smart actuation will not be available on the X-56A, so this report investigates the use of trailing-edge control surfaces for shape control.

Presented in this report is a robust control law design methodology for stabilizing X-56A aircraft models and controlling the wing shapes. The models contain all six rigid-body degrees of freedom (DOF), flexible modes, and ten control surfaces and flight actuators. To use the FOS, the methodology requires implementation of a least-squares estimation (LSE) modal filter. In previous work (ref. 15), the LSE modal filter was tested on a clamped aeroelastic plate model, reinforced with spars and ribs and controlled by two trailing-edge control surfaces. In that work, simulated shape data at the sensor locations was used for sensor inputs to the shape controller. Here, we utilize simulated fiber optic sensor (SFOS) measurements for the shape controller. We derive strain modes from the deformation mode shapes and use these modes for both modal estimation and strain simulation.

The use of spatial filtering (that is, modal filtering) and distributed sensing enables practical shape control. Point sensors such as strain gages or accelerometers could be utilized to support shape control. But arrays of point sensors must be frequency-filtered or placed optimally to capture important modal coordinates of interest, or both (ref. 16). Distributed sensors with modal filtering do not introduce unwanted dynamics into the problem, and the modal displacement estimates will be resistant to the effects of residual modes (refs. 15, 17, and 18).

Three objectives are achieved in this report. The first objective is to verify that the modal filter is a valid estimator for an aircraft. The second objective is to show that virtual deformation control (see ref. 15) on an aircraft in flight is achievable. This is accomplished with SFOS feedback (ref. 8) and trailing-edge control surface effectors. The third objective is to show that a controller designed to incorporate a modal filter can be made to be robust to structured uncertainties and speed variations. We demonstrate that the popular $\mu$-optimal approach (refs. 19 and 20) can be used to design a modal controller which achieves multiple-input multiple-output robust stability and performance.

## The X-56A Model

The wings of the X-56A model are fitted with four trailing-edge control surfaces. There are two body flaps on the rigid center body. All of these control surfaces are available to the controller for both AFS and flight control. The medium-sized unmanned aerial vehicle aircraft will be operated in experimental studies at subsonic speeds and at low altitude. A top-down view of the X-56A aircraft is shown in figure 1.

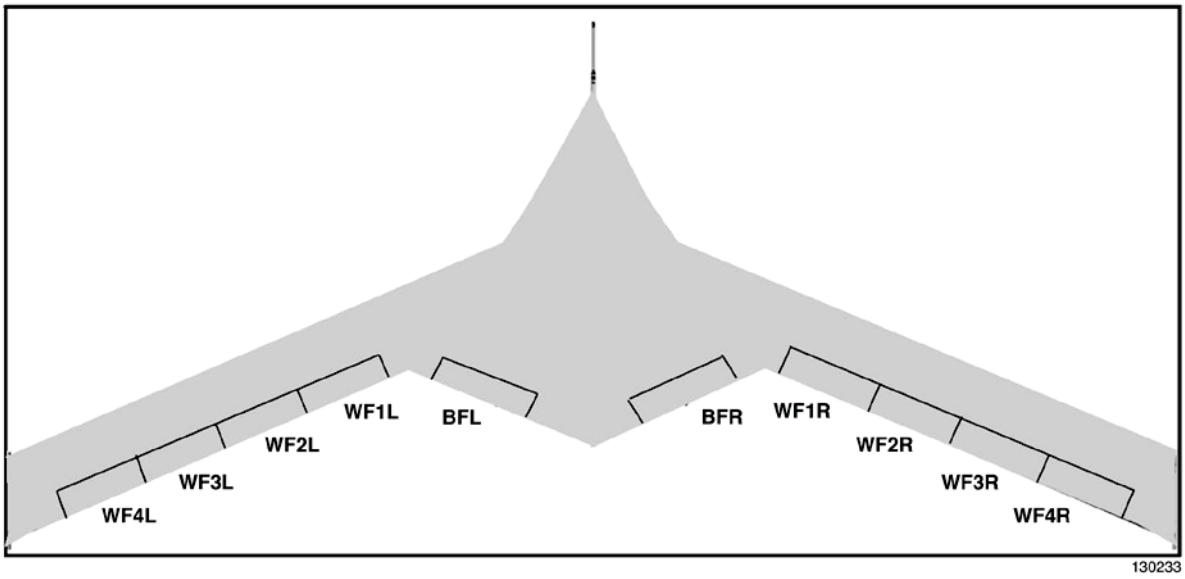


**Figure 1. Top-down configuration of the X-56A (L: left; R: right) (figure courtesy Lockheed Martin, Bethesda, Maryland).**

To simulate fuel in the wings for a passenger transport aircraft, water tanks are included on each wing. This generally makes control design more difficult because the controller will either need to adapt or be robust to the varying modal properties. This challenge may be compared to the wing stores AFS problem of the Northrop YF-17 airplane (ref. 21). For simplicity, the simulation model used here assumes that the water tanks are empty. The aircraft has no rudder, so its yaw control will be limited. To yaw, the control surfaces must move in opposing directions to generate more drag on one side of the vehicle. To identify the flutter characteristics of the vehicle, a normal modes analysis is first completed.

## Normal Modes Analysis

The normal modes analysis was completed in MSC Nastran™ (ref. 22) (MSC Software Corporation, Newport Beach, California) on a detailed finite element model (FEM) developed by Lockheed Martin. The FEM corresponding to the water-empty case was utilized. The detailed FEM is shown in figure 2.

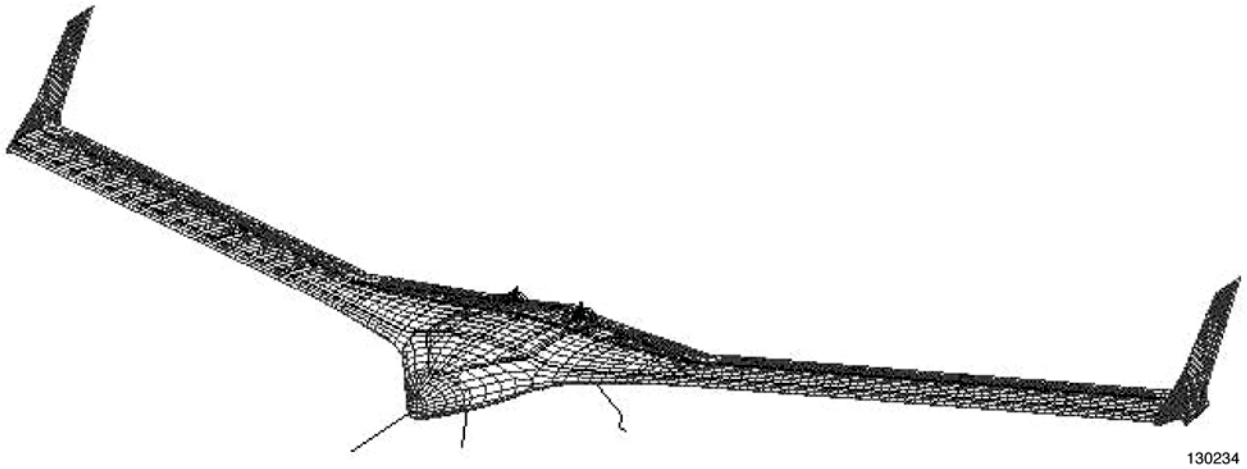


**Figure 2. The finite element model of the X-56A aircraft.**

The FEM contains over 6,000 nodes. The FEM has not yet been updated through a ground vibration test. For model development and flutter analysis, the modes were computed in MSC Nastran™ using the Lanczos eigensolver. The modes are shown here amplified by a large amount (for visualization) in figure 3.

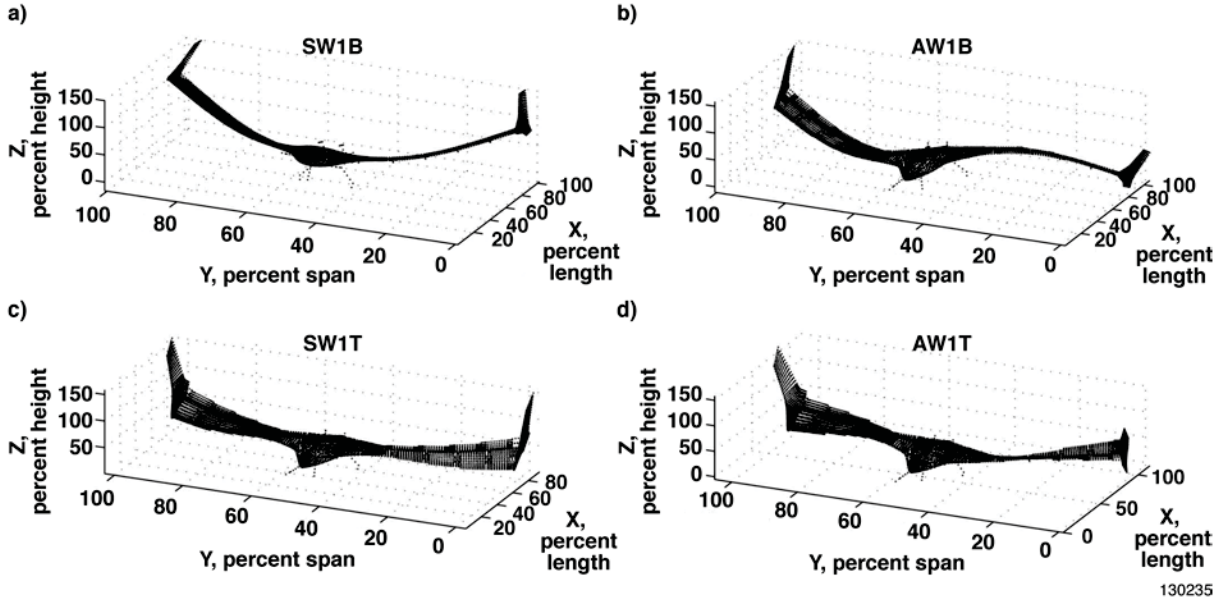


**Figure 3. Normal mode shapes: a) SW1B; b) AW1B; c) SW1T; and d) AW1T.**

Only four modes are shown here, but 14 flexible modes were included in all of the X-56A models. Fourteen were found to be sufficient to capture the salient flexible motion characteristics. Visual inspection reveals that the first two mode shapes appear to be strongly coupled with rigid-body motion. The coupling is pronounced in the symmetric wing first bending (SW1B) mode, where rigid-body pitch and heave are observed. The antisymmetric wing first bending (AW1B) mode has a substantial rigid-body roll component. The symmetric wing first torsion (SW1T) mode has a slight pitch coupling which is difficult to see. The antisymmetric wing first torsion (AW1T) is slightly coupled with roll. The flutter analysis presented below elucidates how the modes couple in flight.

## Flutter Analysis

To determine the theoretical flutter margins of a vehicle the eigensolution of the aeroelastic system equation is solved (ref. 2) as shown in equation (1):

$$M\ddot{q}(t) + J\dot{q}(t) + Sq(t) = \frac{1}{2}\rho_\infty V_\infty^2 Q q(t) \tag{1}$$

where $M \in \mathbb{R}^{m\times m}$ is the generalized mass matrix, $J \in \mathbb{R}^{m\times m}$ is the generalized damping matrix, $S \in \mathbb{R}^{m\times m}$ is the generalized stiffness matrix, $Q \in \mathbb{R}^{m\times m}$ is a generalized aerodynamic force (GAF) matrix, and $q(t) \in \mathbb{R}^{m\times 1}$ are the modal displacements of the vehicle. The aerodynamic interaction of the modes with the structure is captured by the GAF matrices. For flutter analysis, the GAFs must be converted from individual frequencies to Laplace domain. To achieve this, the GAF matrices, $Q$, are computed over a range of reduced frequencies and are fit in a rational function approximation (RFA) as shown in equation (2):

$$\tilde{Q}(s) = A_o + \frac{L}{V_\infty} A_1 s + \frac{L^2}{V_\infty^2} A_2 s^2 + Y \left[ sI - \frac{V_\infty}{L} R \right]^{-1} Es \tag{2}$$

where $A_o$, $A_1$, and $A_2$ are rational approximation matrices, $Y$ and $E$ are rational approximation matrices of lag terms, $R$ is a diagonal matrix of lag roots, $L$ is the characteristic length, and $V_\infty$ is the freestream velocity. Roger's method (ref. 23) with three aerodynamic lag orders was used for the aerodynamic approximation in the ZONA Technology Inc. (Scottsdale, Arizona) ZAERO software package (ref. 24). After substituting equation (2) into equation (1), and performing an inverse Laplace transform, the time domain aerodynamics in the equations of motion is achieved. It is important to verify that the frequency domain aerodynamics match the time domain aerodynamics for model accuracy. Therefore, in the flutter analysis, both frequency and time domain solutions are presented together in figure 4.

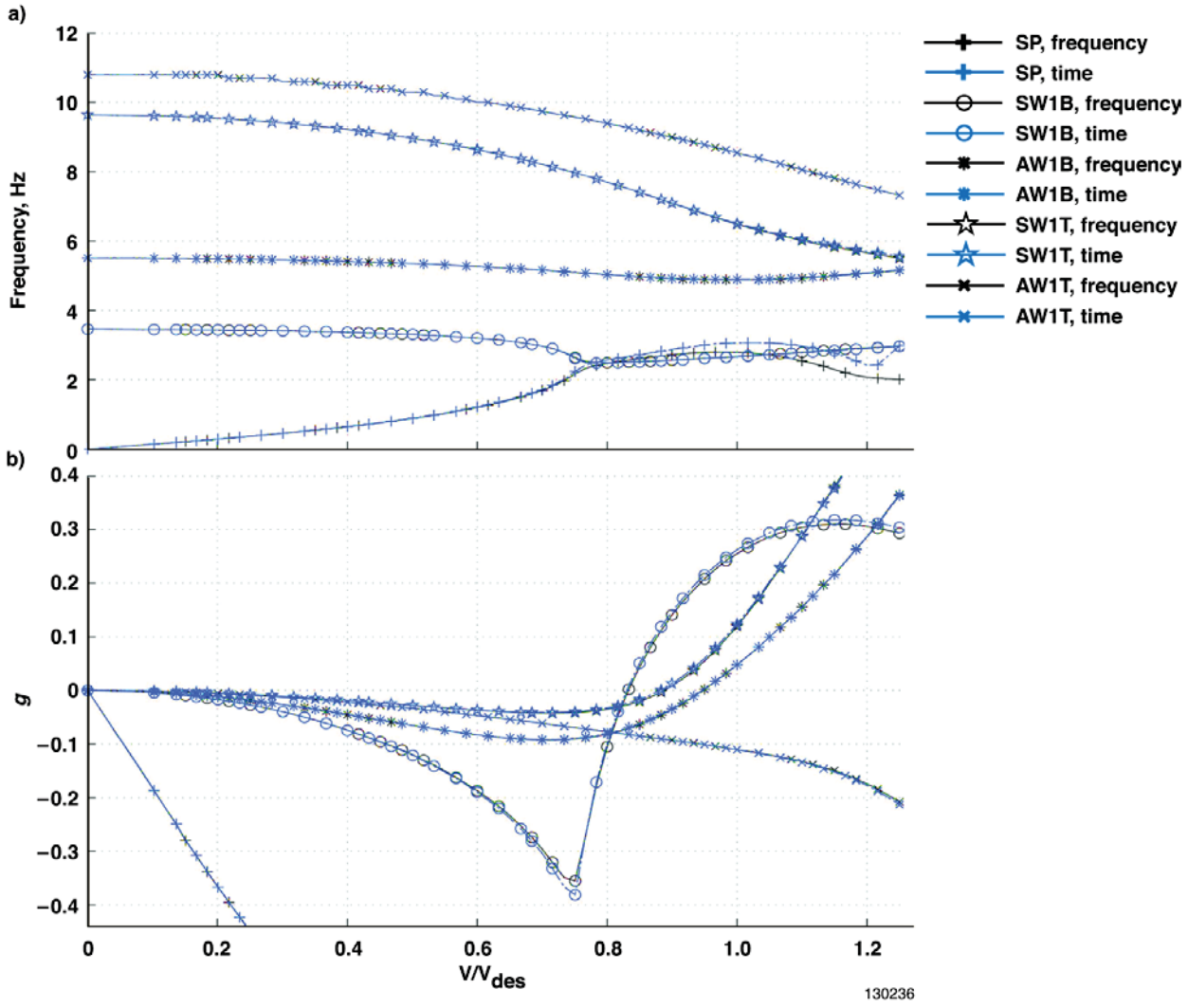


**Figure 4. Flutter analysis: a) velocity versus frequency, V-f ; and b) velocity versus damping, V-g.**

At first glance, figure 4 indicates that the aerodynamic approximation for the state space models matches the frequency domain aerodynamic solutions. The primary purpose of figure 4 is to reveal the

flutter characteristics of the X-56A model. Theoretically, flutter appears at a velocity in the model when the damping, ($g$), goes to 0. In practice, flutter predicted in this way is conservative, as structural damping is unaccounted for.

Figure 4(b) reveals that three flutter modes exist. The first mode that goes unstable (that is, crosses $0g$) is the body freedom flutter mode (BFF) at a ratio of design speed, $V_{des}$ , of approximately 0.82. The BFF frequency is 2.7 Hz (16.9 rad/s). The viscous damping ratio for the BFF is -0.13. Recall that the $g$ value is equal to the negative of twice the viscous damping (ref. 25). Therefore, positive $g$ corresponds to an unstable flight condition. The symmetric wing bending and torsion flutter mode (SWBT) appears at approximately 89 percent of design speed at 6.5Hz (41 rad/s). The viscous damping ratio of the SWBT is lower than the BFF at -0.06. The velocity versus frequency plot, V-f, indicates that unfavorable coupling occurs between the SW1B and SW1T modes, similar to what one might expect when performing a flutter analysis on a clamped plate (ref. 25). Typically, the coupled modes' frequencies shift down but do not coalesce. The antisymmetric wing bending and torsion flutter mode (AWBT) appears at 94 percent of design speed at 4.9 Hz (30.7 rad/s). The damping ratio of the AWBT is -0.024. This represents another unfavorable coupling between the AW1B and AW1T modes.

Figure 4 shows three strong flutter modes in the flight envelope which must be designed for in the active control system. The viscous damping of each mode decreases (becoming more unstable) very quickly, relative to velocity changes. This is especially true for the BFF. The flutter characteristics (damping ratios and frequencies) presented above represent the salient characteristics of the state space models over a range of speed. The development of the X-56A state space models is further discussed below.

## X-56A State Space Modeling

The X-56A aeroservoelastic state space model assumes the matrix time derivative form for simulation and control design shown in equation (3) (see ref. 24 or ref. 26):

$$\begin{aligned} \dot{x}(t) &= Ax(t) + Bu(t) \\ y(t) &= Cx(t) + Du(t) \end{aligned} \qquad x(0) = x_o \tag{3}$$

with the initial state $x(0) = x_o$. The $n$-dimensional vector $x(t)$ is referred to as a state vector and at any discrete time during a simulation can be accessed to give the current "state" of the system. The $o$-dimensional vector $y$ is the system measurements. According to equation (3), only the current state and the $a$-dimensional input $u$ are required to know the state in the next time step. The $A$, $B$, $C$, and $D$ matrices are real constant matrices with $n \times n$, $n \times a$, $o \times n$, and $o \times a$ dimensions. States are not unique to any given system; however, the X-56A state vector is defined as shown in equation (4):

$$x(t) \triangleq \{x_{AF}(t), x_e(t), x_{\dot{e}}(t), x_{lag}(t), x_{act}(t)\}^T \tag{4}$$

where $x_{AF}(t) \in \mathbb{R}^{AS\times 1}$ is a vector of airframe states, $x_e(t) \in \mathbb{R}^{m\times 1}$ is a vector of modal displacements, $x_{\dot{e}}(t) \in \mathbb{R}^{m\times 1}$ is a vector of modal velocities, $x_{lag}(t) \in \mathbb{R}^{f\times 1}$ is a vector of aerodynamic lag states and $x_{act}(t) \in \mathbb{R}^{z\times 1}$ is formed from a vector of actuator accelerations, velocities, and displacements. For the X-56A model, the state space models were calculated at small velocity increments over a range of speed. The resulting models are collected into the aggregate model, $G_V$, to be used later for analysis.

Figure 4 predicts that the design plant $G_{des}$ will be subject to three flutter modes. To verify that these modes are present at the design speed, the X-56A state space model was perturbed with a unit-scaled control deflection command to the right-wing control surfaces (see fig. 1), lasting 0.001 s. The pertinent state space variations are plotted in figure 5.

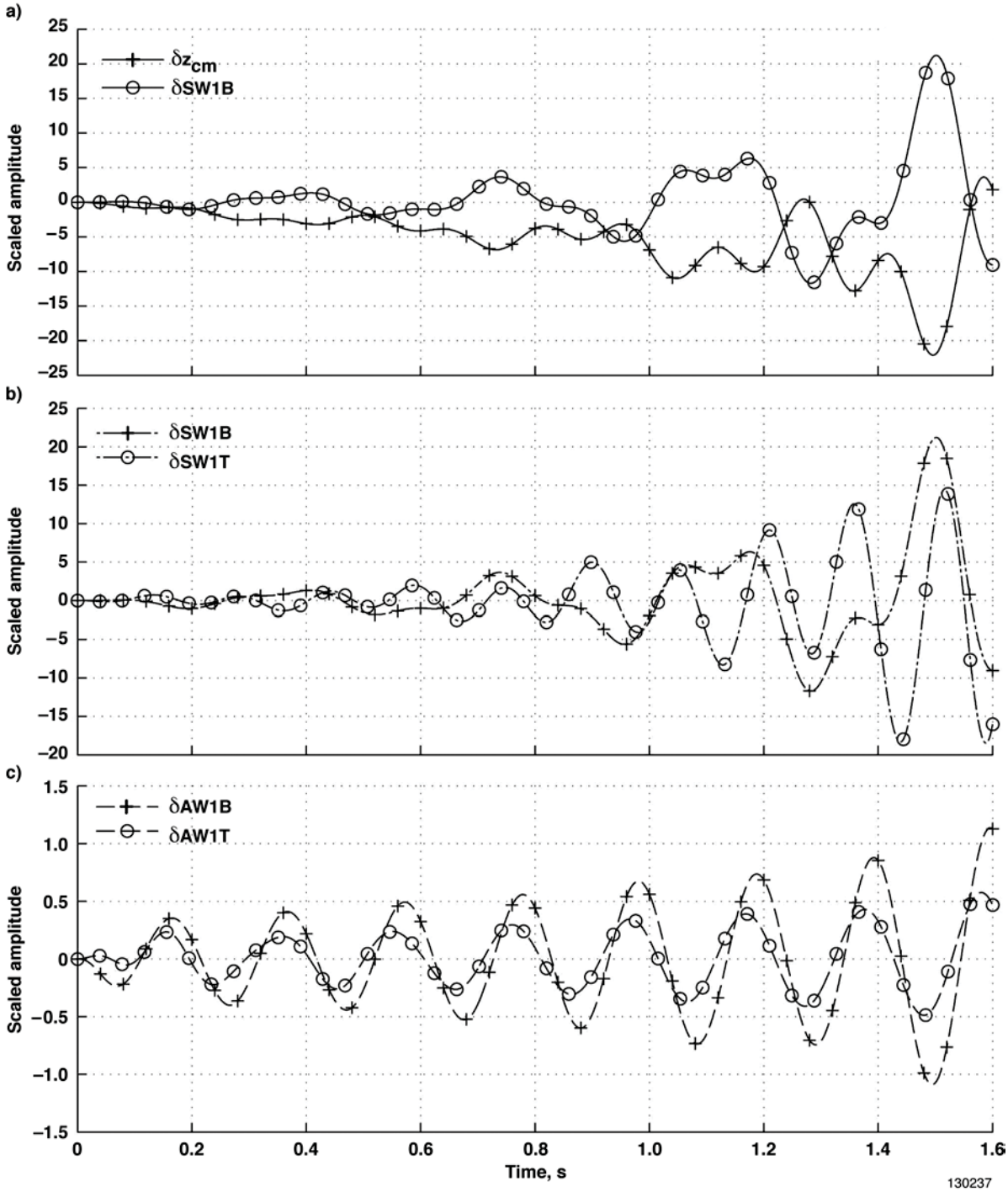


**Figure 5. The X-56A model in open-loop flutter at design speed: a) BFF; b) SWBT; and c) AWBT.**

The BFF in figure 5(a) is demonstrated by the interaction of the scaled states, rigid-body heave state, $\delta z_{cm}$ , and modal displacement $\delta SWB1$. The effect of gravity is also modeled. Note that altitude is lost over time. It is observed that the amplitude of the interacting states increases with time and oscillates at the same frequency, out of phase. The SWBT, figure 5(b), also illustrates the unfavorable coupling of modal displacements: $\delta SW1B$ and $\delta SW1T$. The nature of the coupling is difficult to discern because it appears random in nature. The AWBT, figure 5(c), shows an in-phase interaction of modal displacements:

$\delta AW1B$ and $\delta AW1T$. The scaled modal amplitudes are small but clearly grow in time, verifying that this flutter mode also exists at the design flight condition. Without control, the aircraft is clearly going unstable and will require AFS at a minimum.

# Methodology

The model of the unstable X-56A aircraft was introduced above. Three flutter modes were identified, including BFF, SWBT, and AWBT before the design speed. Active flutter suppression is desired to suppress the flutter modes; however, a higher objective of this work is to sense and command the shape of the aircraft. The available sensors include SFOS and flight sensors. It is shown how the SFOS may be used to estimate the modal displacements with the modal filter. This is followed by incorporating the modal filter into an aircraft shape control design paradigm. The overall methodology is designed to support the simulation framework given in figure 6.

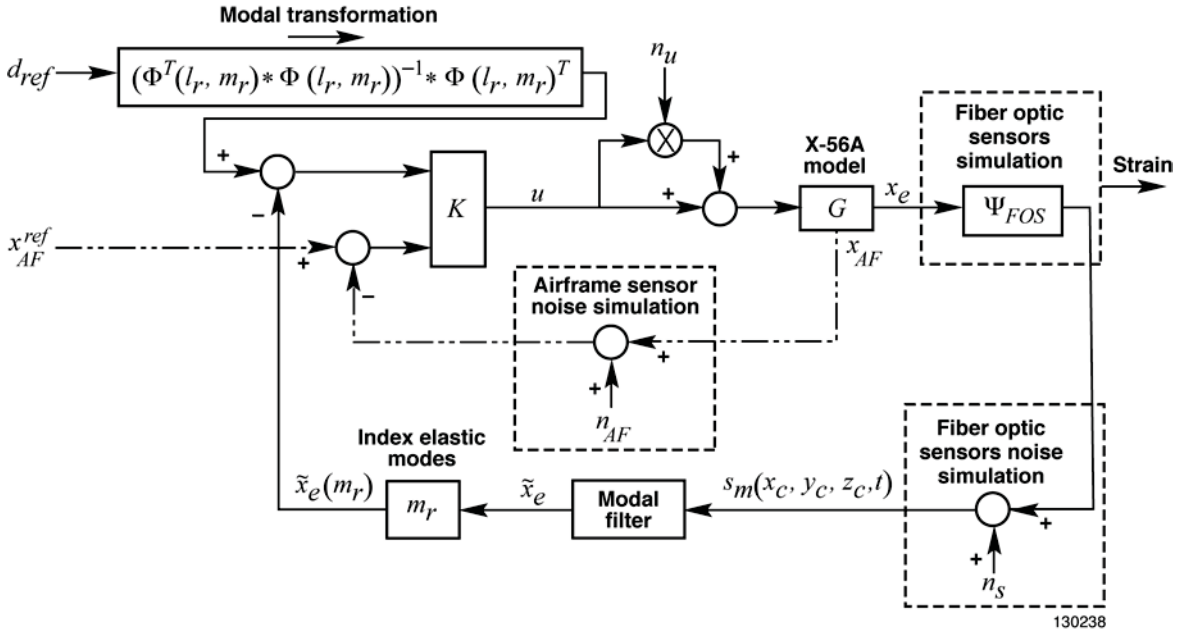


**Figure 6. The virtual deformation control architecture for the X-56A model.**

In this simulation framework, there are three important steps which must be taken. First, the controller, $K$, must be designed. Second, the modal filter and SFOS must be developed; and third, the modal transformation must also be developed, which is used to generate modal displacement reference signals for the shape controller. The methodology below is presented, which supports the simulation shown in figure 6. The connections and variables are more completely described farther on in this report.

## Modal Filtering in the Aircraft State Space Model

The purpose of using the modal filter (see fig. 6) is to estimate the modal displacements of a flexible structure. The modal filter was originally developed for the purpose of developing independent modal control systems, and was reliably found to remove the possibility of exciting residual modes in the control system (ref. 17). In aircraft, frequency-based filters have been traditionally used for this purpose (ref. 4). The first modal filter was derived using the modal expansion theorem (ref. 27), which states that for structures with distinct natural frequencies, the deformation of all nodes of the structure $d(x_C, y_C, z_C, t)$

can be set equal to a linear combination of the natural mode shapes of the structure $\{\phi_i(x_C, y_C, z_C), i = 1 \ldots N\}$ as shown in equation (5):

$$d(x_C, y_C, z_C, t) = \sum_{i}^{N} q_i(t)\phi_i(x_C, y_C, z_C) \tag{5}$$

The mode shapes are made orthogonal to the mass matrix, and are thus orthogonal to each other. The orthogonality property makes residual modes invisible to the estimator. Thus, it achieves spatially-filtered estimates without corruption from residual modes if enough sensors are available (ref. 18). The highly-distributed nature of the SFOS is why the SFOS so naturally support modal filtering. Strain has a similar relationship, which has been used to define the strain-based modal filter. The relationship of the strain-based modal filter to the modal displacement state vector $x_e(t)$ is defined in equation (6) (see refs. 28 and 15):

$$x_e(t) = (\Psi^T\Psi)^{-1}\Psi^T s_m(x_C, y_C, z_C, t) + \varepsilon \tag{6}$$

where $\Psi = \{S_d\phi_i(x_C, y_C, z_C), i = 1 \ldots N\}$ is a $N \times N$ strain matrix with $N$ strain modes, $s_m(x_C, y_C, z_C, t) \in \mathbb{R}^{N\times 1}$ is the strain and $\varepsilon$ is the error. This represents the modal filter in its pseudo-inverse form (ref. 28). Since the modal filter gives a partial state estimate of the full state vector, $x(t)$, the form of the output matrix is simply identity for measured modes.

The sensor output matrix, $C$, is a matrix of row vectors relating the sensory information to the state vector, $x(t)$. Previously (see ref. 15) the output matrix was developed for the case of a rectangular wing, where rigid-body motion was restrained. Here, the output matrix is adjusted for rigid-body state feedback concurrent with modal deformation state feedback. It is assumed that only $m$ modes are retained for measurement. Similar to before, the output matrix is formed assuming all modal displacements, $x_e$ , and rigid-body states, $x_{AF}$ , are measured, as shown in equation (7).

$$C \triangleq \begin{bmatrix} I_{AS\times AS} & 0_{AS\times m} & 0_{AS\times m} & 0_{AS\times f} & 0_{AS\times z} \\ 0_{m\times AS} & I_{m\times m} & 0_{m\times m} & 0_{m\times f} & 0_{m\times z} \end{bmatrix} \tag{7}$$

Measuring all flexible states (or rigid states) is not required to adequately sense the vehicle state. Modes which are unstable and contribute strongly to the deformation of the structure are good candidates. Higher-order modes generally do not significantly contribute strongly to the deformation (refs. 16 and 17). These modes may be cautiously ignored to reduce the size of the $C$ matrix. An excellent method for choosing which modal displacements to feed back is that of identifying interacting modes from the flutter analysis presented in figure 4. Modes which interact strongly and lead to flutter are important to the feedback control system (ref. 15). One may also look at the modal mass of each mode to determine which modal displacements will be significant to the response (ref. 15). A convergence study (ref. 29) may be useful for choosing which modes to feed back to control a fluttering structure.

## Incorporation of Modal Filtering into Aircraft Control System Design

Described above was how the modal filter may be incorporated mathematically into the state space model, which is in turn used for control design. The modal filter implementation was also demonstrated in figure 6. The implementation of the modal filter is split into phases. The phases suggested here include: the control design phase, the modal filter design phase, and the shape reference signal design phase.

A methodology for incorporating a modal filter was given in reference 17, however, it was not specific to an aircraft or for shape control. The phases are presented as follows:

*1. Control Design: Phase I*

1) Define the robustness and performance requirements.
2) Identify which modes are significant to the response of the model, through the flutter analysis (see fig. 4).
3) Update the output matrix to measure the identified modes in the state space model as in equation (7).
4) Scale and reduce the order of the plant.
5) Design the controller, K , with the chosen control synthesis technique.
6) Reduce the controller order.
7) Verify that the performance and robustness requirements were met, while simulating the controller on a range of plants around the design plant.
8) Iterate steps 2 through 7.

*2. Modal Filter Design: Phase II*

1) After selecting the modes for feedback, place the sensors either using an optimal sensor placement (ref. 30) technique or intuition of which modes are being measured.
2) Form the sensor strain modal matrix, $\Psi_{FOS}$ .
3) Select an operator to calculate the modal displacements with the modal matrix.

*3. Shape Reference Signal Design: Phase III*

1) Identify the reference points on the vehicle for shape tracking, using the optimal sensor placement techniques or intuition.
2) Correct the elastic mode shapes to remove the rigid-body translations or rotations, if any.
3) Form a modal set-point transformation matrix with the corrected mode shapes.
4) Verify that the flexible modes included in the controller lead to acceptable deformation control. If they do not, include more modes in the controller for integral tracking within the actuator bandwidth and repeat the control design phase.

Depending on the platform in which the modal filter is implemented, some of the steps may not need to be taken. For example, if a plant is small enough, order reduction may not be required. During reference signal construction for a less-flexible structure, flexible modes may not be coupled with rigid-body translation and rotation. These modes will not need correction.

## Control Design

The methodology defines the way the modal filter fits into an aircraft shape control design paradigm. It was shown that only simple changes were required for the state space matrices to utilize the modal filter; see equations (6) and (7). To design the controller as stated in Phase 1, the actual fiber optic sensor locations need not be determined yet; only the modal displacements which are desired to be controlled should be known. The requirements of the vehicle controller are now derived, and a μ-optimal controller is designed, which can track both rigid-body states and the first two modal displacements.

## Control Design Overview

It is desired to suppress the flutter modes (see figs. 4 and 5) and track the rigid-body commands of the X-56A aircraft. In addition, one of the primary objectives is to demonstrate virtual deformation control on a flight vehicle. To this end, the contributing structural modal displacements will be tracked. In this regard, the shape of the aircraft will be controlled. The following discussion will be primarily concerned with how Phase I was accomplished. The first step of Phase I is to define the robustness and performance requirements.

Since flutter is a potentially destructive phenomenon, the modal controller must be robust to uncertainty. This is especially important for a modal controller, since during a ground vibration test, mode shapes are typically not predicted exactly (ref. 16). In fact, cross-coupling is a primary argument against using a modal filter for control. Cross-coupling can occur when any one mode shape in the modal matrix is not accurate and propagates into other modal displacement estimates through projection (ref. 31). To reduce these uncertainties, the following uncertainty requirements were defined: 10 percent multiplicative uncertainty on the inputs and outputs, and 10 percent additive uncertainty on the scaled plant. Since flutter speeds are hard to predict precisely and structural damping is not modeled, the controller requirements must also be satisfied at off-design conditions. A notional requirement is that the controller must be robust to a 3-percent speed variation. Since the flutter mode damping decreases so rapidly with speed variations (see fig. 4), this requirement is seen as practical.

Robustness to parameter uncertainty is highly desirable, but the controller must also meet performance specifications. The tracked measurements must respond to doublet inputs with low rise times and small overshoots. The performance must also be achievable under the aforementioned uncertainty conditions. The uncertain plant and required control system is summarized in figure 7.

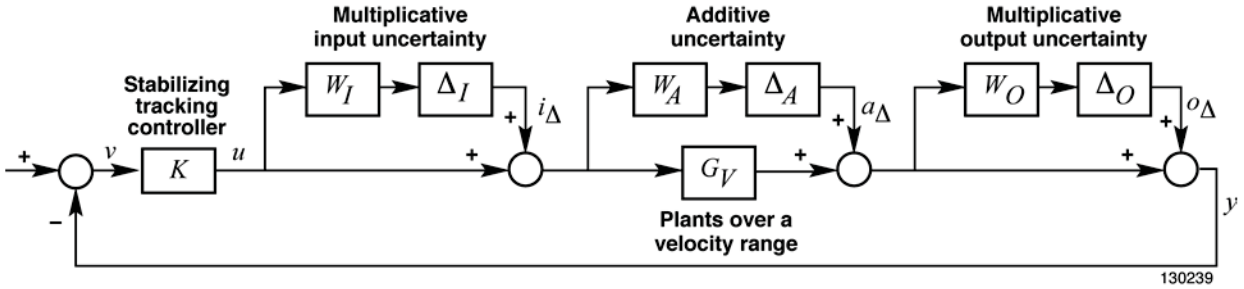


**Figure 7. The uncertain plant and the required controller.**

With the uncertainties in figure 7 in mind an $\mu$-optimal control approach was taken (ref. 19). The design approach uses a hybrid of performance weights and uncertainty weights. Robust stability (RS) is achieved if and only if a system is stable for all perturbed plants about the nominal model up to the worst-case uncertainty (ref. 19). The robust stability condition which must be met for the $\mu$-optimal controller is shown in equation (8).

$$RS \iff \mu\big(M_\Delta(\hat{\imath}\omega)\big) < 1, \forall\omega \tag{8}$$

The $\mu$ is calculated over the frequency range with the relation shown in equation (9) (see ref. 19):

$$\mu\big(M_\Delta(\hat{\imath}\omega)\big) = \frac{1}{min\{k_m | det(I - k_m M_\Delta(\hat{\imath}\omega)\Delta) = 0 \; for \; structured \; \Delta, \bar{\sigma}(\Delta) \leq 1\}} \tag{9}$$

where $k_m$ is the stability margin, $\bar{\sigma}$ is the maximum singular value, and $\Delta$ is the structured uncertainty. The transfer function matrix from the input of the uncertainty blocks to the outputs of them as shown in figure 7 is presented in equation (10):

$$M_\Delta = \begin{bmatrix} -W_I T_I & -W_I K S_O & -W_I K S_O \\ W_A S_I & -W_A K S_O & -W_A K S_O \\ W_O G S_I & W_O S_O & -W_O T_O \end{bmatrix}, G\mathcal{E}G_V \tag{10}$$

where $W_I$ is a matrix of proper input weights, $W_A$ is a matrix of proper additive weights, $W_O$ is a matrix of proper output weights, and $K$ is the controller. From this matrix, the salient sensitivity and complementary sensitivities from the $M_\Delta$ structure are identified which correspond to the requirements. The magnitude of the singular values predict the performance of the control system. These closed-loop transfer functions are defined in equation (11) (see ref. 19):

$$\begin{aligned} T_I &= KG(I+KG)^{-1} \\ KS_O &= K(I+GK)^{-1} \\ S_O &= (I+GK)^{-1} \\ S_I &= (I+KG)^{-1} \\ T_O &= GK(I+GK)^{-1} \end{aligned} \tag{11}$$

where $\boldsymbol{T_I}$ is the input complementary sensitivity, $\boldsymbol{S_O}$ is the output sensitivity, $\boldsymbol{S_I}$ is the input sensitivity, and $\boldsymbol{T_O}$ is the output complementary sensivitiy. To improve rejection of control input uncertainty, the controller was designed around the plant as shown in figure 8.

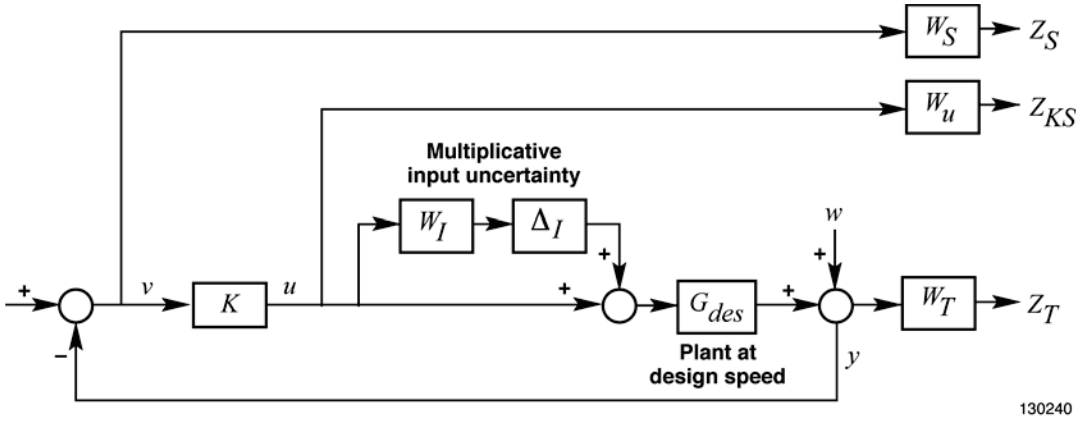


**Figure 8. The control design framework.**

The design plant, $G_{des}$ , at the design speed, $V_{des}$ , was of order 130. To improve controller synthesis, $G_{des}$ was scaled by the full range of actuator movement and expected sensor output changes (see ref. 19). The translational states, $\delta x_{cm}$, $\delta y_{cm}$, and $\delta z_{cm}$, and the velocity state were removed from the model. With the resulting 126th-order model, balanced reduction (ref. 32) was performed to bring the model order to 90 states. The selected states to be tracked were: $SW1B$ and $SW1T$ modal displacements; pitch angle, $\theta$; and bank angle, $\phi$. The angle of attack, $\alpha$; angle of sideslip, $\beta$; yaw angle, $\psi$ ; and a body accelerometer were also sensed but were chosen to be suppressed.

Traditional proper weights from a mixed $\boldsymbol{\mathcal{H}_\infty}$ synthesis were utilized, along with multiplicative uncertainty at the plant inputs. The input uncertainty weight, $\boldsymbol{W_I}$, was adjusted to achieve maximum amplitude near the actuator break frequency. Sensitivity weight, $\boldsymbol{W_S}$, was adjusted for integral tracking on tracking states and for suppression on suppression states. It was found that the break frequencies of the modal displacement performance weights had to be increased 10 rad/s relative to the airframe state weight break frequencies of 1 rad/s. The break frequency of the control weight, $\boldsymbol{W_u}$, was adjusted to 5 rad/s for reduced control surface movement. The break frequency of the complementary sensitivity weight, $\mathbf{W_T}$, was set to 30 rad/s to improve high-frequency noise rejection. The uncertainty transfer function, $\mathbf{N_\Delta}$, was calculated (see fig. 8) to be as shown in equation (12):

$$N_\Delta = \begin{bmatrix} W_I T_I & -W_I K S_O \\ -W_S G S_I & -W_S S_O \\ -W_u T_I & -W_u K S_O \\ W_T G S_I & -W_T T_O \end{bmatrix} \tag{12}$$

One may verify that all of the pertinent closed-loop transfer functions corresponding to those shown in equation (11) are present in equation (12). Thus, by reducing the $\mathcal{H}_\infty$ norm of $N_\Delta$, the robustness will increase and it will be easier to meet the specified requirements (see fig. 7). For this control design architecture, the $\mu$-optimal controller was computed using the MATLAB® (The MathWorks, Inc., Natick, Massachusetts) Robust Control Tool Box. To find the controller, DK-iteration (see ref. 19) was performed, which solves the iterative optimization problem shown in equation (13):

$$\min_K \left( \min_{D_\omega} \left\| D_\omega N_\Delta(K) {D_\omega}^{-1} \right\|_\infty \right) \tag{13}$$

The DK-iteration resulted in a 162th-order controller after some trial and error with the weights in figure 8. The controller was then internally balanced (ref. 32) and truncated to 44 states without a substantial loss of robustness or performance. This resulted in an $\mathcal{H}_\infty$ norm of 3.29. It was difficult to meet both performance and robustness requirements with the scaled plant. Therefore, the desired $\mathcal{H}_\infty$ norm of 1 was not achieved. Rescaling may improve the controller.

Nominal stability (NS) was verified for the reduced-order controller by verifying that eigenvalues of the closed-loop system had real negative parts. An analysis of the singular values of the open-loop plant and controller as well as the closed-loop sensitivity functions given in equation (11) are presented in figure 9.

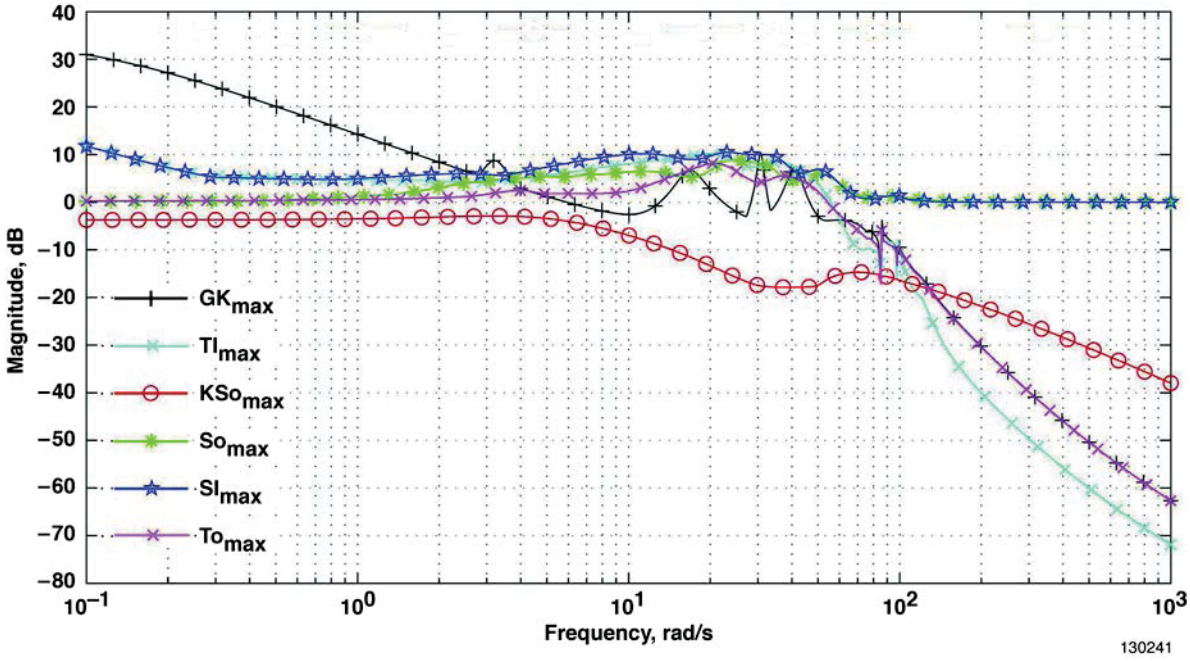


**Figure 9. Maximum singular values of open-loop (GK) and closed-loop sensitivity functions.**

At first glance, figure 9 reveals that most of the closed-loop transfer functions stay at or beneath 10 dB, corresponding to a magnification of the inputs to these transfer functions of approximately 3.2. The controller bandwidth is 25 rad/s, which is below the actuator break frequency. After this frequency, the complementary sensitivities fall sharply at 60 dB/decade. Therefore, noise will be attenuated well past 25 rad/s.

Recall that it is desired that the controller be robust to uncertainty and, of course, disturbances. Robustness to input multiplicative uncertainty is strongly impacted by the maximum singular values of $T_I$; see equation (10). The maximum singular value of $T_I$ within the bandwidth of the controller has a magnitude of 10 dB. Therefore the controller will amplify input uncertainties at frequencies where flutter is most likely to occur.

Robustness to additive uncertainty or gust responses is strongly affected by the peak of the closed-loop transfer function, $KS_O$. Over the entire bandwidth, the singular values of $KS_O$ are below 0 dB and, thus, gust-like disturbances will be attenuated. The magnitude of the singular values of $KS_O$ falls off quickly after 6 rad/s. This predicts that higher-frequency turbulence will be rejected.

Robustness to sensor uncertainty is predominantly dependent on the peaks of $S_O$ and $T_O$. From 0.1 rad/s to 1 rad/s the singular values of $S_O$ show that plant uncertainty is neither amplified nor reduced; however, near flutter frequencies the plant uncertainty is amplified. The singular values of $T_O$ indicate that sensor noise or output uncertainty will not be strongly amplified past 25 rad/s.

Some aspects related to tracking may also be identified from figure 9. For best tracking accuracy, $T_O$ must be equal to 0 dB over most of the controller bandwidth. Figure 9 shows that there are several peaks above 0 dB, which may lead to overshoots or poor performance. The tracking history can be investigated by inputting doublet reference inputs to the controller. The set of charts presented in figures 10-12 expands on the performance and robustness characteristics of the controller.

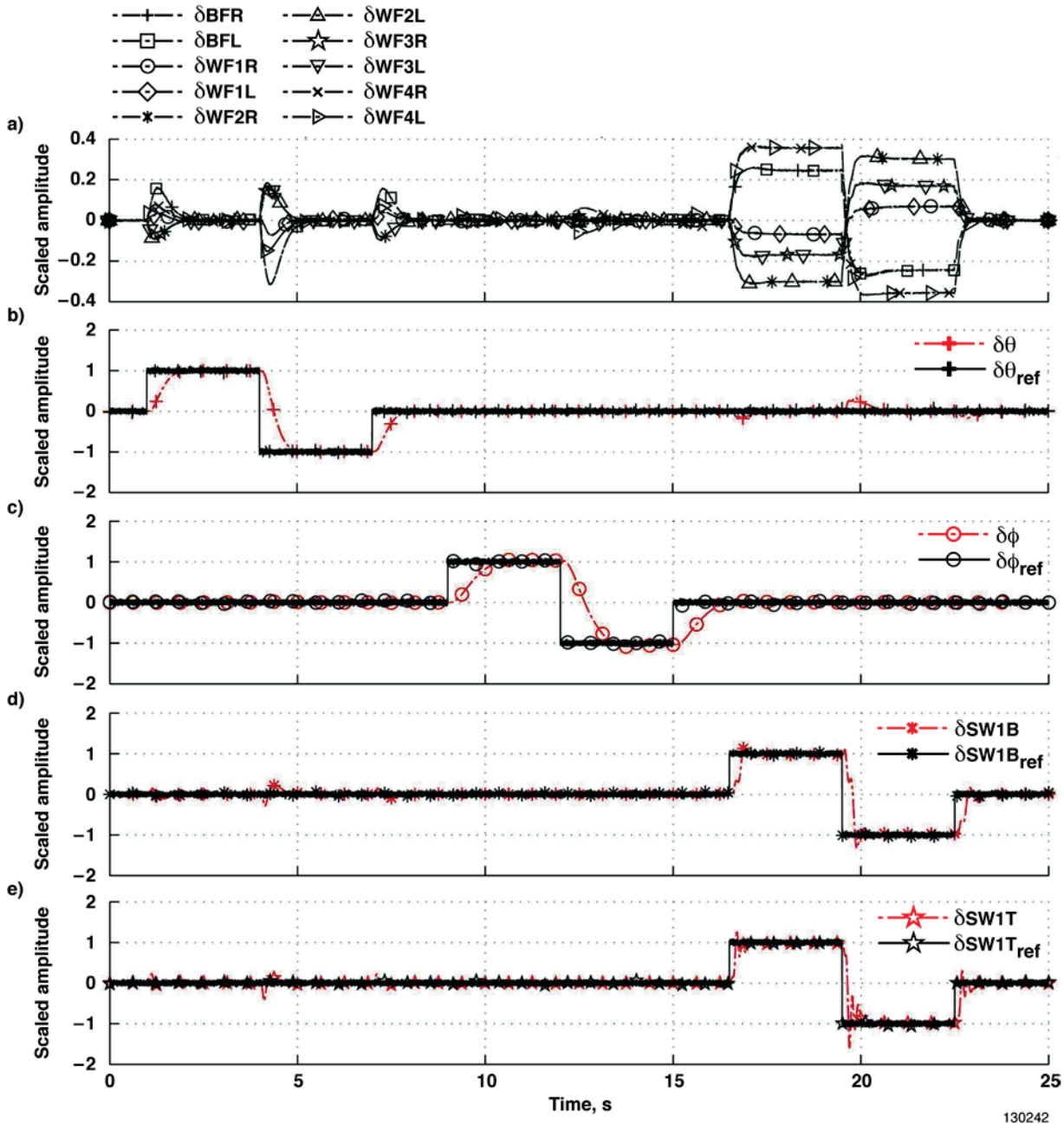


**Figure 10. Performance chart for doublet inputs to tracked variables: a) control surfaces; b) pitch angle tracking; c) bank angle tracking; d) SW1B modal displacement tracking; and e) SW1T modal displacement tracking.**

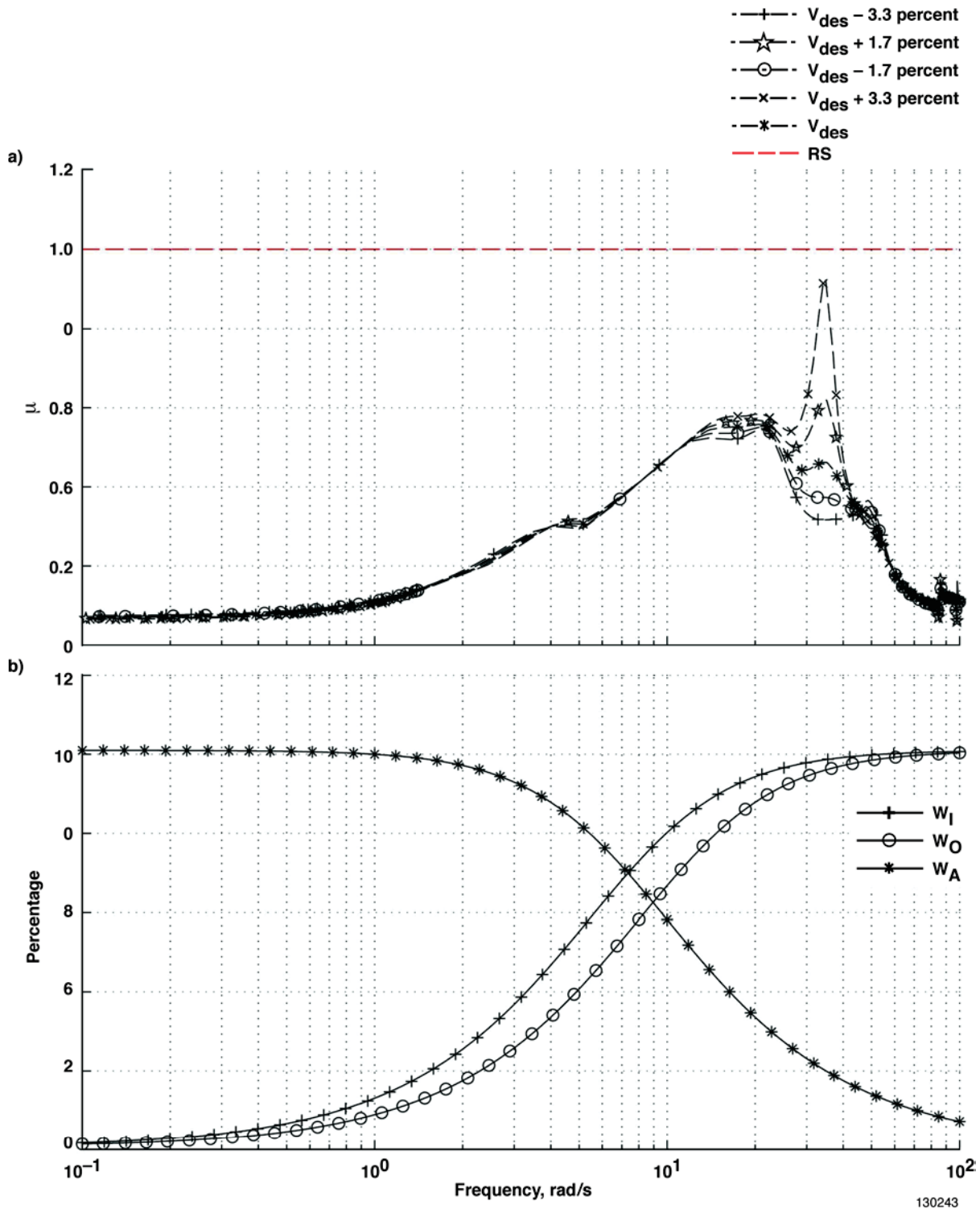


**Figure 11. Mu analysis over speed range: a) $\mu$ chart; and b) corresponding uncertainty weightings.**

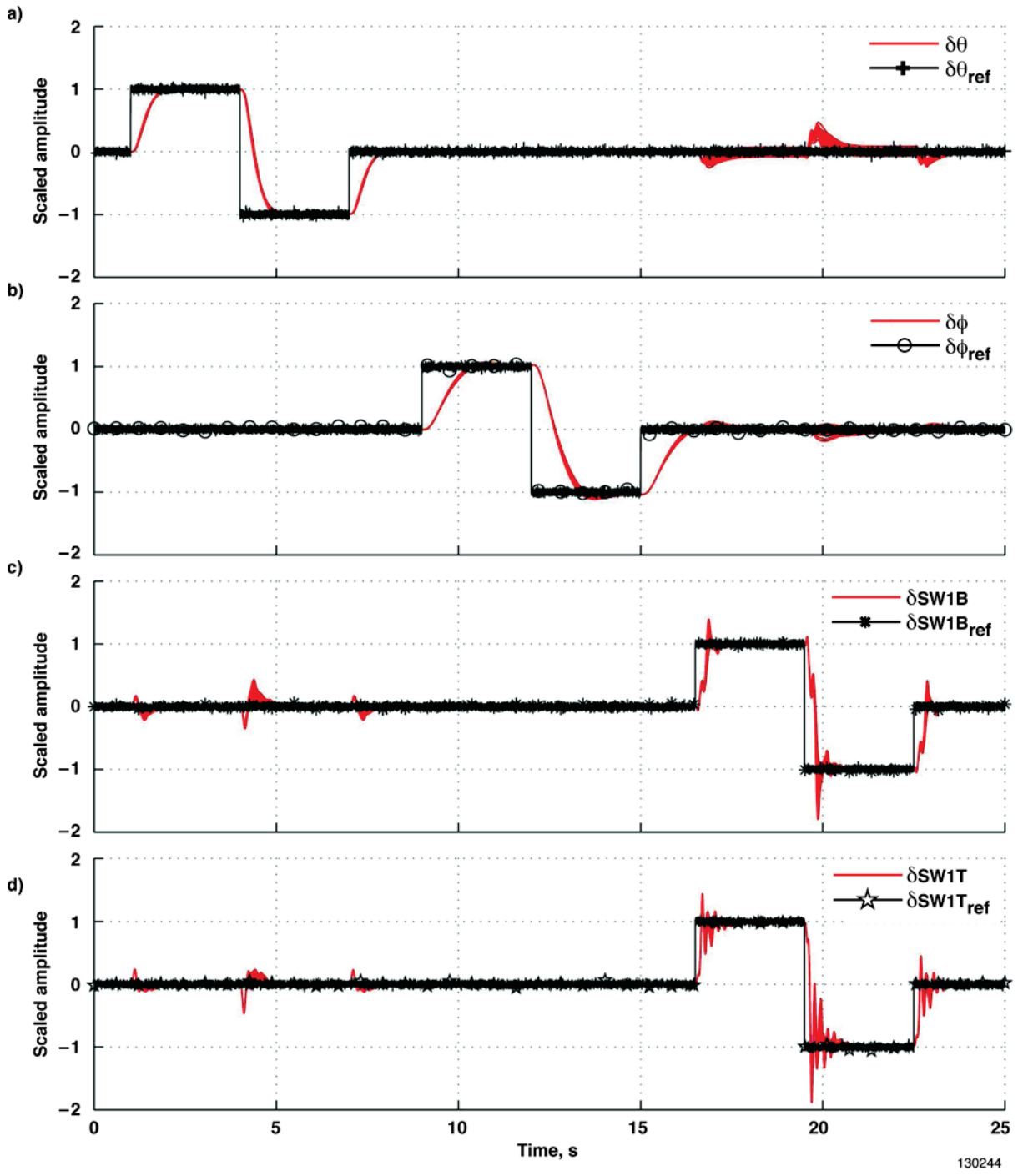


**Figure 12. Performance over 3.3% variation of velocity and uncertainty range: a) pitch angle tracking; b) bank angle tracking; c) SW1B modal displacement tracking; and d) SW1T modal displacement tracking.**

It was desired that the responses of the system to a doublet have low rise time and small overshoots. This goal was for the most part achieved (see figs. 10 and 12). All of the signals had low rise times of 0.25 s to 1.5 s. The change in pitch angle, $\delta\theta$, had excellent tracking characteristics. The change in bank angle, $\delta\phi$, showed a reasonable response. The tracked modal displacements were non-minimum phase.

The modal displacement, $\delta SW1T$, experienced a 25-percent overshoot, which was predicted by the singular values of $T_O$.

There was very little rigid-body longitudinal and lateral coupling. It was interesting that the commanded rigid-body signals moved off their reference point when modes were commanded. The converse also happened; pitch angle commands tended to disturb the modal displacements. This indicates that a strong coupling between rigid-body motion and flexible motion in the models exists, which cannot be easily avoided.

The normalized control movements for $\delta\theta$ and $\delta\phi$ tracking were reasonably small. In fact, the movement of the control surfaces for $\delta\phi$ tracking was almost unnoticeable. During modal displacement commands, the normalized control movements moved to a maximum amplitude of 0.4 on the body flaps. Since the outputs are scaled to half of the actuator limits, this is a relatively large control movement, but is not unreasonable. In figure 10(a) it can be seen that the normalized control movement was significantly larger when commanding the modal displacements, than when commanding the flight variables. Significant control authority is required to perturb the X-56A structure from equilibrium; however, improper scaling may be to blame. Based on this analysis, the nominal performance (NP) appears to be adequate, although it might be improved with better weights and plant scaling.

Figure 9 indicates that some disturbances and uncertainties are amplified; however, the actual impact of these uncertainties on the stability must be checked with a $\mu$ analysis as shown in figure 11. The $\mu$ analysis calculates robustness of the modal controller across dimensions of speed and uncertainty. For a range of plants $G_V$ additive, multiplicative input and output uncertainties with 10 percent weightings was added; see figure 11(b). The chosen shapes of the weightings were meant to replicate worst-case scenarios. Additive uncertainties may be more likely to occur in the 0.1 rad/s to 10 rad/s range due to gust disturbances. Multiplicative uncertainties may be more likely to occur at higher frequencies due to actuator dynamics and sensor uncertainties and noise. For the generalized plant with uncertainties, $\mu$ were then calculated across the operational frequency range with one controller, as shown in figure 11(b).

Recall that RS is guaranteed if the condition given in equation (8) is met. Therefore, it is desirable that $\mu$ be less than one for all structured uncertainties. The maximum $\mu$ for all perturbed plants was 0.92. Therefore, RS is achieved. The variation of $\mu$ across the frequency range shows that it tended to increase at closed-loop flutter mode frequencies. The $\mu$ tended to increase for speeds past the design speed. Conversely, the $\mu$ decreased for plants below the design speed. This happens because as speed increases the damping of the flutter modes decreases; see figure 4(b). The reverse happens when decreasing in speed. Figure 11 indicates that the design requirement to be RS to a 3-percent variation in speed was met. Hence, it is shown here that the modal controller can be designed to be a robust to modeled uncertainties. Performance at off-design conditions must also be analyzed.

Robust performance (RP) is achieved if and only if the performance objectives are achieved for all possible plants about the nominal plant up to the worst-case uncertainty (ref. 19). There were no hard performance requirements defined other than that the tracked signals have low rise times and small oscillations. Figure 12 indicates that the responses from the perturbed plants were tight around the acceptable nominal plant responses shown in figure 10. The overshoots on the modal displacements for some perturbed plants did increase to 50 percent, but this overshoot increase is acceptable for the current study. Therefore, RP is achieved for these lenient performance requirements. Since NP, RP, NS, and RS are adequately achieved, the modal controller is acceptable. It meets basic criteria necessary for utilization in an aircraft. This completes Phase I. The controller designed here is used in the below discussion for virtual deformation control simulation.

## Virtual Deformation Control Simulation

The modal controller derived above adequately satisfies the robustness and performance objectives for the X-56A model. The simulation study presented here demonstrates the use of the modal filter for virtual deformation control of the aircraft. To complete Phase II, the simulated fiber optic sensors are placed on

the X-56A FEM. The sensor strain modes are calculated and the sensor strain mode matrix is formed. It is then shown that in order to create a proper deformation signal for Phase III, rigid-body translations and rotations must be removed from the deformation mode shapes. An objective function is given, which is minimized to achieve this goal. For demonstration, the controller designed in Phase I is put into a simulation with the modal filter designed in Phase II. The wing tips are commanded to a particular deformation using the reference signal derived in Phase III.

## Fiber Optic Sensor Placement

Traditionally, strain sensors or accelerometers used for active structural control are placed in an optimal sense. The FOS can measure strain at locations that are less than a one-half-inch apart, and can contain several thousand measurement stations along a single fiber. One of the benefits of having so much spatial sensor resolution is that optimal sensor placement (OSP) routines (refs. 30 and 32) lose significance. The first few structural modes in bending and torsion are most significant to flutter, so the sensors are placed from root to wing tip to capture bending information. The sensors are laid from trailing edge to leading edge to capture torsional motion. The resulting sensor configuration looks like three claw marks across each wing. The resulting sensor configuration is given in figure 13.

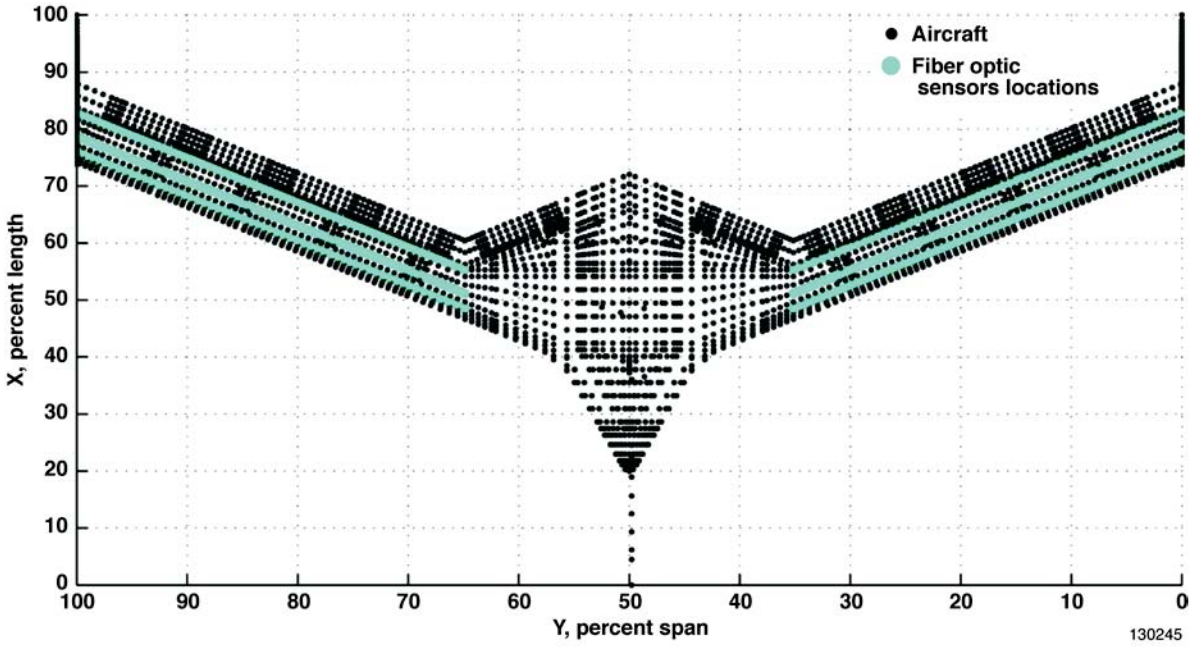


**Figure 13. The fiber optic sensor layout on the X-56A model.**

With the six fibers placed, points on the aircraft were also chosen where deformation could be commanded with the reference signal derived in Phase III. These points can be anywhere on the aircraft (see ref. 15). A multitude of points could have been chosen, but for simplicity four points were selected. While not required, an OSP technique, known as Kammer's effective independence (EI) procedure (ref. 33), was utilized to locate the four points. This procedure starts by forming a sensor projection matrix from a selection of mode shapes. In this case, the sensor deformation mode shapes were utilized. The rows of the modal matrix were iteratively reduced based on the smallest diagonal of the projection matrix. After implementing this procedure, the resulting four deformation command locations were determined and are shown in figure 13.

These points are right-wing trailing edge (RWTE), right-wing leading edge (RWLE), left-wing trailing edge (LWTE), and left-wing leading edge (LWLE). Their index locations in the modal matrix are referred

to as $\boldsymbol{l_r}$. As in previous work (ref. 15) results indicate that the wing tips carry the most modal information. Note that the selected points do not have to be on sensor locations for the virtual deformation concept to be employed.

## X-56A Sensor Strain Modes

The strain and deformation modes defined at the SFOS locations are necessary to develop an operational modal filter. To model sensor locations on the model, a spline was made on existing nodes on the FEM in MSC Nastran™ from root to tip on the wing. The distance between each node on the spline was set at one-half-inch, which was the spacing between each measurement grating on the fiber (ref. 8). At each node of the spline or sensor location a minute mass was added. The sensor nodes on the spline were then interpolated with RBE3 MSC Nastran™ cards. The modal analysis conducted in MSC Nastran™ gives sensor deformation mode shapes corresponding to each flexible mode.

The close proximity of the sensors (of approximately one-half-inch) along the SFOS gives a unique opportunity to calculate axial strain modes directly from the modal deformation at the sensor locations. To our knowledge, this is not a common practice. It is also possible to calculate the strain-displacement relation using the finite element method (ref. 34) which may be more reliable for complex structures. One might also perform a static strain analysis for each deformation mode shape to obtain a strain mode shape. For simplicity, the following technique is utilized to convert each sensor deformation mode shape from MSC Nastran™ to a strain mode shape. Recall the axial strain in an element (ref. 35), where $x_l$ is in the direction of the strain measure, shown in equation (14):

$$\varepsilon_{xx} = \frac{\partial u}{\partial x_l} \tag{14}$$

The FOS measure axial strain, so it is assumed that $x_l$ is in the local coordinate direction of the SFOS layout. Figure 14 is presented as a visual aid for the breakdown of equation (14) into a usable format.

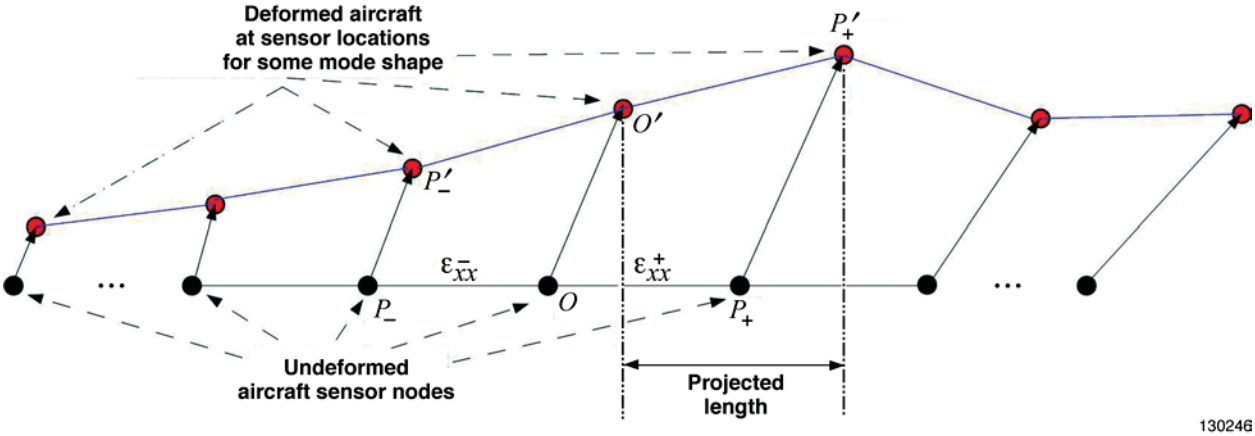


**Figure 14. The fiber optic sensor locations deformed for notional mode shape.**

Figure 14 represents sensors from the SFOS along the aircraft wing, which have been labeled for clarity. Each sensor has a line drawn between it, where a fictitious isotropic beam is assumed to exist. The deformed sensors are connected with blue lines. The original sensors are connected with black lines. Consider the deformed fictitious beam, to be in blue. Linear algebra may be used to show that the strain in any fictitious beam element of the SFOS shown in figure 14 is calculated as shown in equation (15):

$$\varepsilon_{xx} = \frac{Proj_{\vec{u}(\overrightarrow{OP})}\overrightarrow{O'P'} - \overline{OP}}{\overline{OP}} \tag{15}$$

where $\overrightarrow{OP}$ is a directed line segment from the un-deformed sensor location $O \epsilon \mathbb{R}^3$ to the un-deformed sensor location $P \epsilon \mathbb{R}^3$, and $\overrightarrow{O'P'}$ is a directed line segment from the deformed sensor location $O' \epsilon \mathbb{R}^3$ to the deformed sensor location $P' \epsilon \mathbb{R}^3$ and $\vec{u}$ is the unit vector. The projection in figure 14 calculates the final length of the beam section with respect to its original beam orientation. The difference between the original length and the deformed length, divided by the original beam length, gives the strain in the beam element. The strain in one beam may differ from the strain in the beam next to it. The strain from modal deformation on the $r^{th}$ sensor (or sensor location $O$) may be defined to be the average of the strain on either side (see fig. 14) as shown in equation (16):

$$\varepsilon_r(s) \triangleq \frac{1}{2}[\varepsilon_{xx}^{+} + \varepsilon_{xx}^{-}] = \frac{1}{2}\left[\frac{Proj_{\vec{u}(\overrightarrow{O_sP_+})}\overrightarrow{O_s'P_+'} - \overline{O_sP_+}}{\overline{O_sP_+}} + \frac{Proj_{\vec{u}(\overrightarrow{O_sP_-})}\overrightarrow{O_s'P_-'} - \overline{O_sP_-}}{\overline{O_sP_-}}\right], s\varepsilon S \tag{16}$$

where $\varepsilon_{xx}^{+}$ is the axial strain measured on the fore side of the sensor and $\varepsilon_{xx}^{-}$ is the axial strain measured on the aft side of the sensor. This operation can be carried out for each mode and at each sensor node, and strain modes $\psi_m$ may be formed by repeating equation (16) for each sensor. The sensor strain modes that result are collected into the desired strain mode matrix defined at SFOS sensor locations, as shown in equation (17):

$$\Psi_{FOS} \triangleq [\psi_1, \psi_2 \dots \psi_i \dots \psi_m] \tag{17}$$

To compute the strain at point $O$ with good precision, candidate sensor locations $P_+'$ and $P_-'$ must be selected close to the original sensor. Since the change in strain was so small between two adjacent sensors, two sensors were selected a few inches away from the desired sensor location. Even with this technique, the resulting strain modes from equation (16) appeared noisy. Thus, the strain was fit to a polynomial surface for each wing and an M-estimator (ref. 36) was utilized to trim outliers. The first four sensor strain modes used for the X-56A simulation studies are given in figure 15.

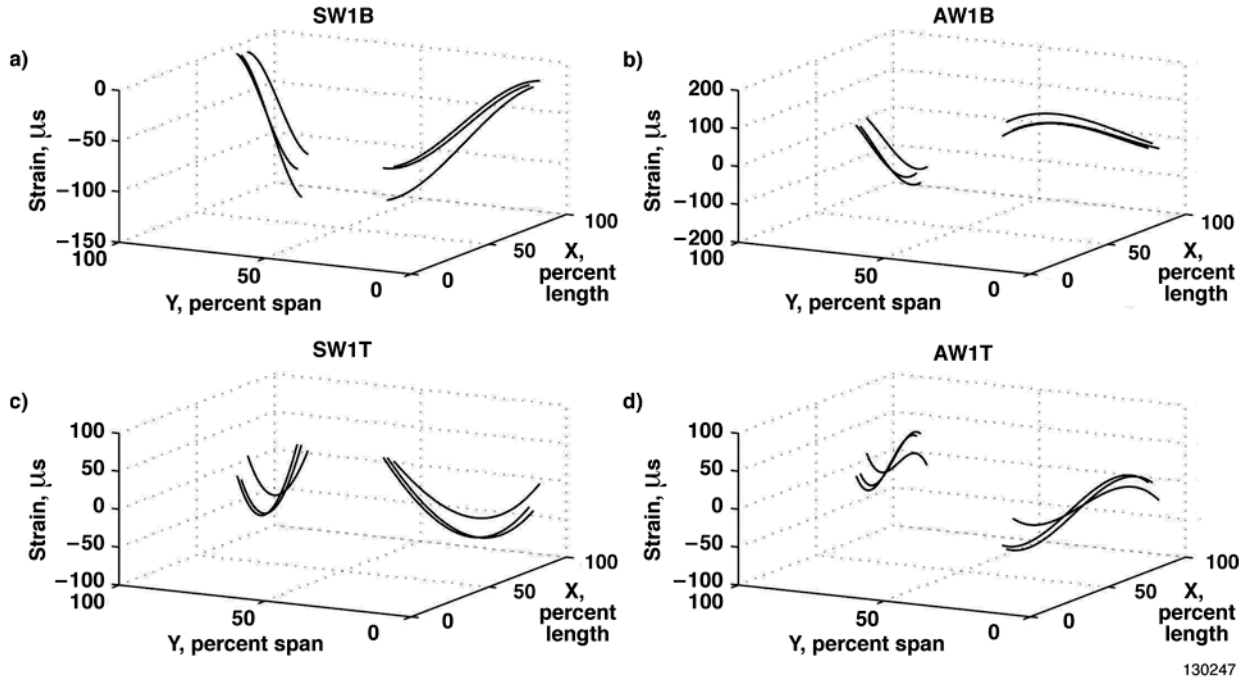


**Figure 15. Sensor strain mode shapes: a) SW1B; b) AW1B; c) SW1T; and d) AW1T.**

The sensor strain modes were computed for all 14 flexible modes of the X-56A, however, only the first four modes are shown here. The SW1B mode has a strain distribution which starts out very high near the root of the wing (see fig. 15) and goes to nearly zero at the wing tips. It is typical that in bending, strain is highest near the root of the beam (ref. 16). The AW1B mode shows an antisymmetric strain distribution in bending. The SW1T mode shows a distribution of strain which has an inflection near zero close to the mid-span of the wing, indicating that for torsion modes where the wing is twisting, very little strain exists in the mid-span of the wing. The AW1T mode, like the AW1B, mode has an antisymmetric strain distribution in torsion. The sensor modes are collected into the modal matrix defined in equation (17) and, together with equation (6), the modal states of the aircraft can be measured. With the strain mode matrix prepared, attention is turned to the reference signal, which is needed for virtual deformation control. For reference signal creation, the deformation mode shapes shown in figure 3 must be transformed.

## Reference Signal Creation

Phase III from the modal filter control design methodology is to design a modal reference command. From equation (5) a least-squares approximation may be used and the modal reference command is shown in equation (18) (see ref. 15):

$$q_{ref} = \left(\Phi^T(l_r, m_r)\Phi(l_r, m_r)\right)^{-1}\Phi^T(l_r, m_r)d_{ref} \tag{18}$$

where $d_{ref}$ is a vector of deformations from the un-deformed aircraft corresponding to the index vector, $l_r$, in the pure elastic deformation modal matrix, Φ. Recall that each row of the modal matrix corresponds to a physical location on the aircraft, $(x_C, y_C, z_C)$. The index of modes, $m_r$ , corresponds to the index of modes within the modal matrix, which the controller is designed to track. In this case, $m_r$ corresponds to {1,3}, since the SW1B and SW1T modal displacements are tracked.

Performing virtual deformation control on the X-56A model is not straightforward because the flexible modes of the vehicle are not purely elastic. The normal mode shapes (see fig. 3) are corrupted by strong rigid-body motion. The use of these modes to recreate the modal reference signal will lead to large displacement errors. The mode shapes required in equation (18) are calculated by an optimization procedure on the original mode shapes. The optimization procedure rotates and translates every node in the mode shape about the aircraft center of gravity (cg).

Recall that a mode shape corresponds to deformations at $N$ grid points. At each grid point, the mode shape is defined for six DOF, so each mode shape technically has $6N$ DOF. The number of DOF is increased with global DOF parameters so the total DOF in each mode equate to $6N + 6$ DOF. The global DOF are the only variables in the objective function defined for the $i^{th}$ mode shape given by equation (19):

$$F_i = \left\| \left\{ \begin{bmatrix} x_{cg} \times 1^T \\ y_{cg} \times 1^T \\ z_{cg} \times 1^T \end{bmatrix} + T(\delta\theta_C)T(\delta\phi_C)T(\delta\psi_C) \begin{bmatrix} \left(x_u + x_\phi^i - x_{cg} \times 1\right)^T \\ \left(y_u + y_\phi^i - y_{cg} \times 1\right)^T \\ \left(z_u + z_\phi^i - z_{cg} \times 1\right)^T \end{bmatrix} + \begin{bmatrix} \delta x_C \times 1^T \\ \delta y_C \times 1^T \\ \delta z_C \times 1^T \end{bmatrix} \right\} - \begin{bmatrix} x_u^T \\ y_u^T \\ z_u^T \end{bmatrix} \right\|_2^2 \tag{19}$$

where $x_{cg}$, $y_{cg}$ and $z_{cg}$ are the scalar coordinates of the cg of the aircraft, $T(\cdot)$ is a right-hand-rotation matrix operator, $x_u$, $y_u$ and $z_u$ are $N \times 1$ coordinate vectors of the un-deformed aircraft, $x_\phi^i$, $y_\phi^i$, and $z_\phi^i$ are $N \times 1$ coordinate vectors of the $i^{th}$ modal deformation vector, $\phi_i$. The six scalar variables in the optimization function include translational coordinates: $\delta x_C$, $\delta y_C$, and $\delta z_C$ , and rotations about all three axes: $\delta\theta_C$, $\delta\phi_C$, and $\delta\psi_C$.

By minimizing the objective function, equation (19), for the $i^{th}$ mode, with respect to these six scalar variables the relative distance between the un-deformed aircraft and the deformed aircraft is minimized. Since the squared Euclidean norm is a strictly convex function of its respective arguments, the objective function is also convex (ref. 37); therefore, there are numerous discrete optimization methods available in the literature which can be used to solve it. For each mode $i$, the objective function is minimized with a locally convergent random search technique known as the compass method (ref. 37). Four of the resulting corrected mode shapes are given in figure 16.

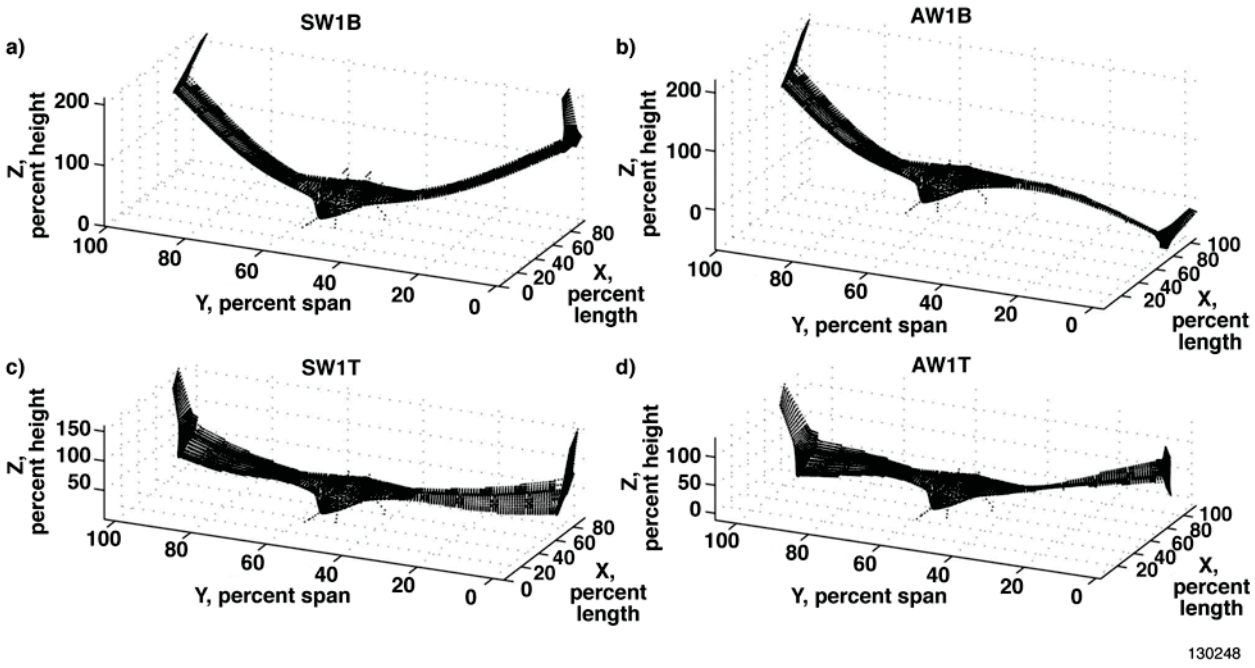


**Figure 16. Corrected mode shapes a) SW1B; b) AW1B; c) SW1T; and d) AW1T.**

The mode shapes with rigid-body components removed (see fig. 16) may be used with equation (18) to develop appropriate reference signals. Note that the flexible movement within each mode appears amplified when compared to figure 3. Deformation commands can now be adequately transformed to achieve virtual deformation control.

## Simulation

The simulation architecture introduced in figure 6 represents the inner-loop design for the X-56A simulation model. The inputs to the controller are references, provided by a notional outer-loop control system. The references in figure 6 are separated into rigid-body commands, $x_{AF}^{ref}$, from the flight computer and vertical deformation commands, $d_{ref}$, at selected locations (see fig. 13), namely, LWLE, LWTE, RWLE, and RWTE. The reference vertical deformations were chosen to be 0.6 percent of the span of the vehicle, which corresponds to modal displacement commands of approximately twice the scaled value. This value was thought to be reasonably small, since the control movement for scaled modal displacement commands was less than 50 percent of the actuator range as shown in figure 10(a).

Since the reference deformations were equal, a bending-type motion for the aircraft wing shape results. Different deformation choices could lead to torsion-type motion instead. The deformation references can be verified to generate a bending motion when transformed with equation (18) into a modal reference. For the following study, the airframe state references are set to 0.

The controller that was designed above (see figs. 9-12) takes the difference of the references and the feedback signals to produce a control input signal. Multiplicative noise is added to the controller inputs, with a mean of 0 and standard deviation of 0.1. The plant takes the inputs via equation (3) and produces the state vector, $x_q$ , in the output, which includes the measurements SW1B, SW1T, and the residual modes. The plant also outputs the rigid-body measurement vector, $x_{AF}$.

The SFOS measurements are simulated by multiplying the sensor strain matrix, $\Psi_{FOS}$ , with the vector, $x_e$. Normal noise, $n_s$ , with mean 0 and a standard deviation of 3 $\mu_s$ is then added to this strain vector. Since the rigid measurements are scaled, a normal distribution with mean 0 and standard deviation of .01

is added to the measurements to simulate noise. The results of the simulation to a reference doublet command are shown in figure 17.

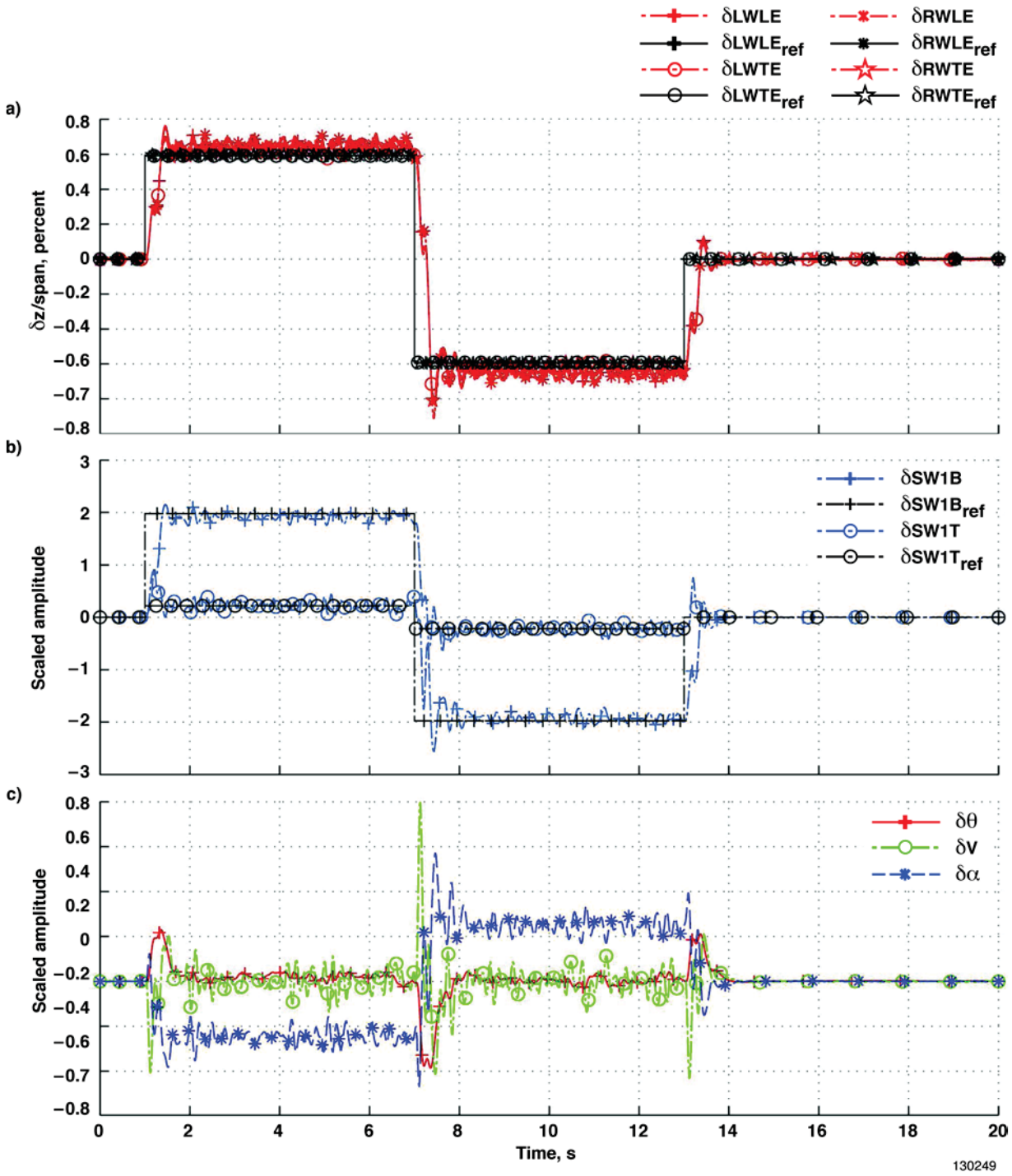


**Figure 17. Virtual deformation tracking time history: a) deformation tracking at wing tips; b) tracked modal displacements; and c) airframe states.**

The change in deformation near the wing tips, figure 17(a), indicates that the actual deformations moved very close to the deformation set-points. The error is due to the modal displacements from residual

modes (see ref. 15). This is expected, since the trailing-edge actuators are not collocated with the structure's sensors. Due to this fact and since the modes are coupled aerodynamically, independent modal control cannot be achieved (ref. 16).

The commanded modal displacements are shown in figure 17(b), and they are tracked well. Since the command is primarily due to bending, the SW1T modal reference is very small. The scaled SW1B modal displacement amplitude moves the greatest amount. Both modes had some overshoot and oscillations during the initial part of the command, which was predicted and is seen in in figure 10. The steady-state response has oscillations primarily due to the rather large multiplicative input noise modeled in the system.

During the shape-deformation maneuver, the aircraft experienced no enduring change of velocity or pitch angle. The angle of attack, however, achieved a steady-state change; the change in angle of attack should have also effected an enduring change in velocity. An angle-of-attack change generally leads to a drag increase or decrease; however, this was not observed, likely due to improper drag modeling. If the results were taken as truth, it could be concluded from this analytical model that the effective lift over drag (L/D) ratio has changed. This observation could be a result of control surface movements, the structural deformation itself, or both. The caveat here is that the results are achieved on a linearized plant model defined for small perturbations around the trim point. In flight, the aircraft achieves a new trim point from the angle-of-attack change, which may result in a lower or higher L/D ratio.

Outer-loop control requirements are also observed from figure 17. The results indicate that the flight-path angle has changed due to shape deformation commands. Therefore, the aircraft will require a heading-angle-hold outer-loop controller to make virtual deformation control feasible. The outer-loop controller could command the pitch angle to control the flight-path angle; or it could command engine throttle settings, which are not currently modeled. If the throttle is changed to achieve trim, fuel efficiency degradation or improvement may be realizable, depending on the command to the structure.

Previously, it was shown that the X-56A model experiences strong flutter at the design speed (see fig. 5). Technically, the shape controller demonstrated above is capable of suppressing flutter. From the previous plots, this has not been shown explicitly. To demonstrate this in a traditional sense, the aircraft is perturbed as before and the control system is turned on after a period of time of 1.6 s. To reduce control-induced oscillations, it was ramped in over a 1-s period, with all references set to 0. In 2 s, the shape tracking controller achieves AFS, as shown in figure 18.

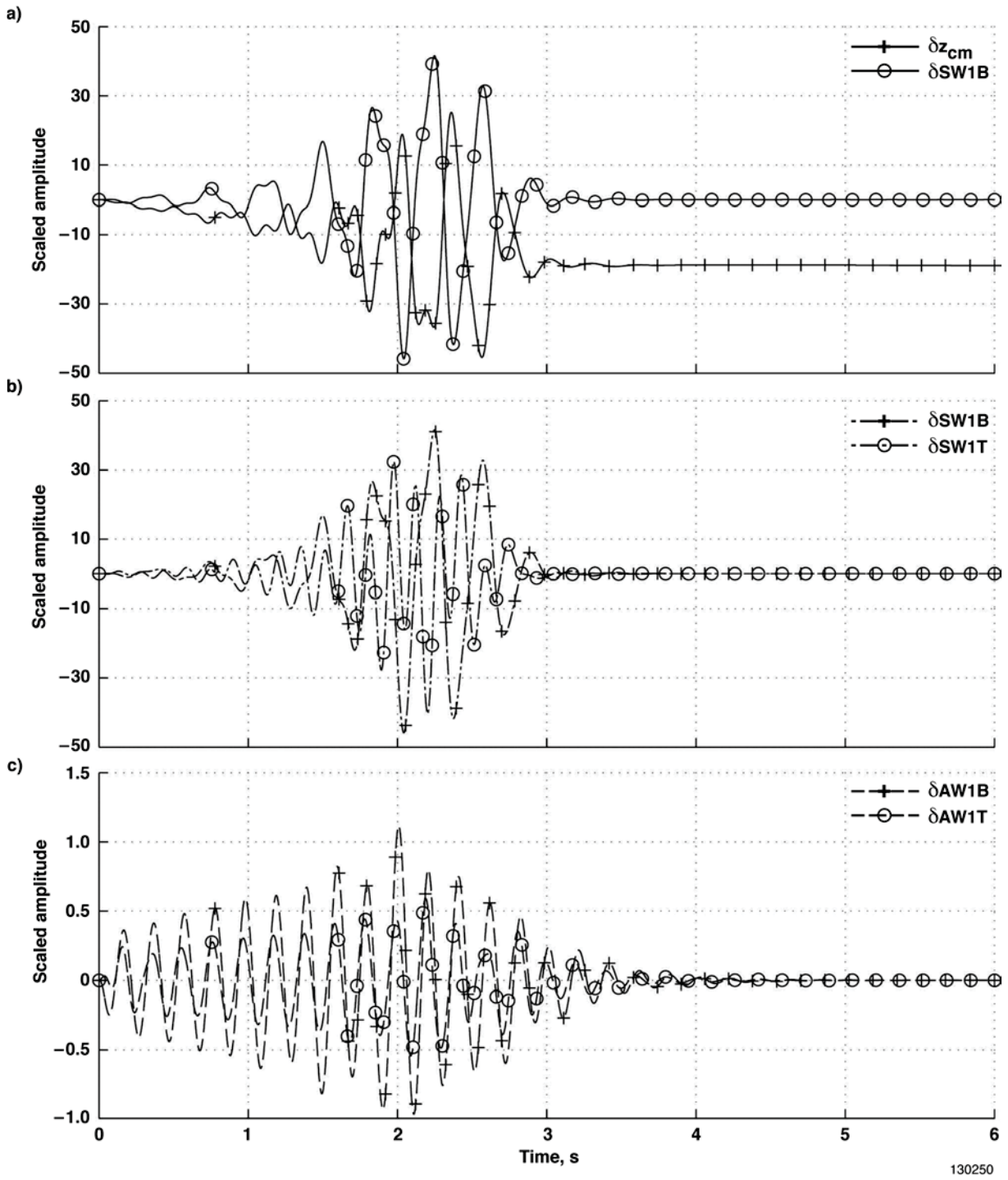


**Figure 18 Active flutter suppression time history: a) BFF suppression; b) SWBT suppression; and c) AWBT suppression.**

During AFS there was an altitude change, as can be seen in figure 18(a); however, this change occurred because an outer-loop guidance system is not currently modeled. The achieved flutter suppression was not unexpected, since control was implemented on a linear plant model. Nonlinear effects have not been included. Only the poles must be considered in such a model. The poles of the

closed-loop system have real negative parts and the closed-loop system is, thus, stable. The open-loop poles and the closed-loop poles are plotted together in figure 19.

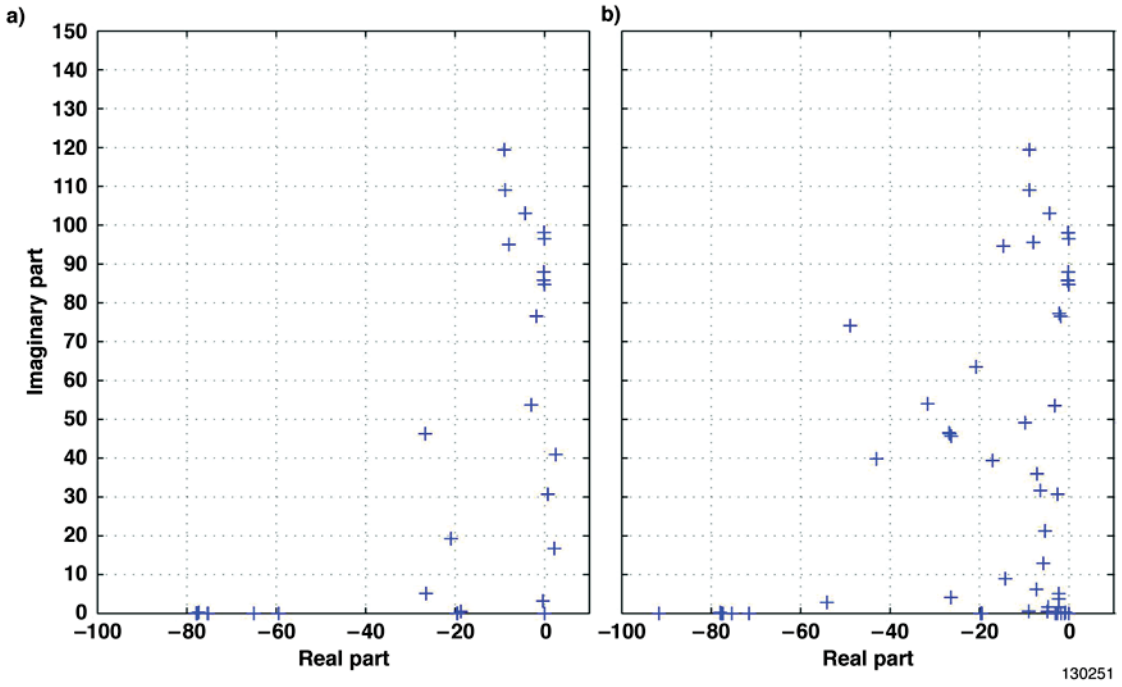


**Figure 19. Open-loop versus closed-loop poles: a) open-loop poles; and b) closed-loop poles.**

The poles of the open-loop system indicate the presence of the three flutter modes identified above (see fig. 4). There are also poles from lightly-damped structural modes near the vertical axis starting at 54 rad/s. When the loop is closed with the controller, the flutter poles migrate to the stable region in the left half-plane. The lightly-damping structural mode poles remain unchanged, as they are outside the controller bandwidth. The controller introduces poles seen tightly grouped near the lower right-hand corner of figure 19(b). Integrator and estimator poles are present. The lowest damping of the closed-loop system poles within the actuator bandwidth is 0.08. This represents a significant improvement over the open loop BFF damping of -0.13.

The results of all simulations must be accepted as notional. Recall that all of the simulations are completed on a linear plant model with simulated strain measurements. Further work with time-marching nonlinear simulations will be necessary to validate the controller architecture for AFS and active shape control; however, these preliminary simulation results are promising. Time histories indicate that the modal filter is a suitable estimator for both AFS and virtual deformation control. Simulation results similar to this were published previously in reference 15, but those results were for a clamped-wing model only.

## Conclusions and Recommendations

There were three primary objectives set out to be accomplished in this report. The first objective was to demonstrate that the least-squares modal filter is a candidate aircraft modal estimator and that it can be adequately used for control feedback. For practical implementation, three phases for incorporating the modal filter were presented and followed throughout the report. The modal filter was demonstrated with simulated fiber optic sensors. The estimated modal displacements were used for both shape control and active flutter suppression of the X-56A simulation model. It was found that significant angle-of-attack

changes occurred during shape control. The angle-of-attack change may lead to improved lift to drag ratios on the aircraft. Therefore, structural shape control may someday enhance performance in fuel efficiency or maneuvers. The caveat is that it is not known what lift to drag ratio will result at the new trim condition. Nonlinear simulations and experimental studies are required to explore this further.

The second objective was to demonstrate that the modal filter and distributed sensing can be used to control the deformation of the aircraft wing structure in flight. By designing a controller for the modal filter and simulated fiber optic sensors, and commanding the wing-tip deflections, this objective was satisfied. Only bending commands were presented here, however. The deteriorating effects of residual modes may be more prominent with other command shapes. Modeling errors could also appear prominently in a realistic bench case study. In-flight experiments are also required to validate its use for aircraft state estimation and control.

The third objective was to show that the modal controller can be designed to have good performance and be robust to parameter variations. This objective was satisfied by employing the powerful mu synthesis technique. It was shown that the controller had robust performance and was robustly stable to structured uncertainty and model speed variations. The requirements for robust performance were lenient, however, and further improvements can certainly be made here. Future endeavors will extend the controller to be robust to fiber optic sensor failures.

## Acknowledgments

This research was funded by the NASA Aeronautics Research Mission Directorate Subsonic Fixed Wing Project and was approved by Steve Jacobson. Mr. Jacobson, the Dryden Controls Branch Chief; John Bosworth, the X-56A Chief Engineer; Jack Ryan, the X-56A Principal Investigator; Ryan Stillwater, the X-56A Controls Lead; Chan-gi Pak, the creator of the X-56A aeroservoelastic model; and the aeroservoelasticity expert Marty Brenner; have all been excellent advisors in the development of these results.

## References

1. Taminger, Karen, “Technical Challenges to Reducing Subsonic Transport Weight,” AIAA Aerospace Sciences Meeting, January 2012.

2. Karpel, Mordechay, “Design for Active Flutter Suppression and Gust Alleviation Using State-Space Aeroelastic Modeling,” Journal of Aircraft, Vol. 19, No. 3, 1982, pp. 221-227.

3. O'Connel, R. F., and A. F. Messina, “Development of an Active Flutter Margin Augmentation System for a Commercial Transport,” Journal of Guidance and Control, Vol. 3, No. 4, 1979, pp.352-360.

4. Zeng, Jie, Jiang Wang, Raymond de Callafon, and Martin Brenner, “Suppression of the Aeroelastic/Aeroservoelastic Interaction Using Adaptive Feedback Control Instead of Notching Filters,” AIAA-2011-6459, August 2011.

5. Norris, Guy, “Breaking the Flutter Barrier,” Aviation Week & Space Technology, Vol. 174, Issue 5, 2012, pp. 28-29.

6. Beranek, Jeff, Lee Nicolai, Mike Buonanno, Edward Burnett, Christopher Atkinson, Brian Holm-Hansen, and Pete Flick, “Conceptual Design of a Multi-utility Aeroelastic Demonstrator,” AIAA-2010-9350, September 2010.

7. Nicolai, Leland, Keith Hunten, Scott Zink, and Pete Flick, “System Benefits of Active Flutter Suppression for a SensorCraft-Type Vehicle,” AIAA-2010-9349, September 2010.

8. Richards, Lance, Allen R. Parker, William L. Ko, and Anthony Piazza, “Real-time In-Flight Strain and Deflection Monitoring with Fiber Optic Sensors,” Space Sensors and Measurements Techniques Workshop, Nashville, Tennessee, August 2008.

9. Kusmina, S., F. Ishmuratov, and V. Kuzmin, V., “Minimization of induced drag of elastic airplane,” AIAA-2004-4611, August 2004.

10. Pendleton, Edmund W., Denis Bessette, Peter B. Field, Gerald D. Miller, and Kenneth E. Griffin, “Active Aeroelastic Wing Flight Research Program: Technical Program and Model Analytical Development,” Journal of Aircraft, Vol. 37, No. 4, 2000, pp. 554-561.

11. Weisshaar, Terrence A., and David K. Duke, “Induced Drag Reduction Using Aeroelastic Tailoring with Adaptive Control Surfaces,” Journal of Aircraft, Vol. 43, No. 1, 2006, pp. 157-164.

12. Austin, Fred, Michael J. Rossi, William Van Nostrand, Gareth Knowles, and Antony Jameson, “Static Shape Control for Adaptive Wings,” AIAA Journal, Vol. 32, No. 9, 1994, pp. 1895-1901.

13. Ehlers, S. M., and T. A. Weisshaar, “Static Aeroelastic Control of an Adaptive Lifting Surface,” Journal of Aircraft, Vol. 30, No. 4, 1993, pp. 534-540.

14. Hu, Yan-Ru, and George Vukovich, "Active robust shape control of flexible structures," Mechatronics, Vol. 15, No. 7, 2005, pp. 807-820.

15. Suh, Peter M., and Dimitri N. Mavris, “Modal Filtering for Control of Flexible Aircraft,” AIAA-2013-1741, April 2013.

16. Preumont, Andre, *Vibration Control of Active Structures An Introduction*, 2nd ed.; Kluwer Academic Publishers, Dodrecht, The Netherlands, 2002.

17. Tzafestas, S. G., ed., *Applied Control: Current Trends and Modern Methodologies*, Marcel Dekker, Inc., New York, 1993.

18. Preumont, A., Francois, A., De Man, P., and Piefort, V., "Spatial filters in structural control," Journal of Sound and Vibration, Vol. 265, No. 1, 2003, pp. 61-79.

19. Skogestad, Sigurd, and Ian Postlethwaite, *Multivariable Feedback Control Analysis and Design*, 2nd ed., John Wiley & Sons, Ltd, West Sussex, 2005.

20. Zhou, Kemin, John C. Doyle, and Keith Glover, *Robust and Optimal Control*, Prentice-Hall, Inc., Upper Saddle River, NewJersey, 1996.

21. Nissim, E., and I. Lottati, “Active External Store Flutter Suppression in the YF-17 Flutter Model,” J. Guidance and Control, Vol. 2, No. 5, 1979, pp. 395-401.

22. *The NASTRAN Theoretical Manual, Level 17.5*, NASA SP-221(05), 1978.

23. Roger, K. L. “Airplane Math Modeling Methods for Active Control Design,” AGARD-CP-228, 1977.

24. ZONA Technology Inc., *ZAERO Version 8.5 Theoretical Manual*, ZONA Technology Inc., Scottsdale, Arizona, 2011.

25. Wright, Jan R., and Jonathan E. Cooper, *Introduction to Aircraft Aeroelasticity and Loads*, John Wiley & Sons, Ltd, West Sussex, England, 2007.

26. Gupta, K. K., M. J. Brenner, and L. S. Voelker, "Development of an Integrated Aeroservoelastic Analysis Program and Correlation with Test Data," NASA TP 3120; NASA Technical Paper 3120, 1991.

27. Meirovitch, Leonard, *Analytical Methods in Vibrations*, The Macmillan Company, New York, 1967.

28. Kang, Lae-Hyong, Dae-Kwan Kim, and Jae-Hung Han, "Estimation of dynamic structural displacements using fiber bragg grating strains sensors," Journal of Sound and Vibration, Vol. 305, No. 3, 2007, pp. 534-542.

29. Pak, Chan-gi, "Unsteady Aerodynamic Model Tuning for Precise Flutter Prediction," NASA/TM-2011-215963, 2011.

30. Kammer, Daniel C., "Sensor Placement for On-Orbit Modal Identification and Correlation of Large Space Structures," American Control Conference, 1990, pp. 2984-2990.

31. Matsumura, Yuichi, "Spatial Filter Design for Observation Spillover Suppression," 2005 IMAC-XXIII: Conference & Exposition on Structural Dynamics, Orlando, Forida, 2005.

32. Gawronski, Wodek, *Advanced Structural Dynamics and Active Control of Structures*, Springer-Verlag, New York, 2004.

33. Kammer, D. C., "A Hybrid Approach to Test-Analysis-Model Development for Large Space Structures," Journal of Vibration and Acoustics, Vol. 113, No. 3, 1991, pp. 325-332.

34. Lee, Jongho, Hunsang Jung, and Youngjin Park, "Feedback FE model updating using strain mode shapes," ICCAS2002, Jeonbuk, Korea, 2002.

35. Levy, Robert, and William R. Spillers, *Analysis of Geometrically Nonlinear Structures*, 2nd ed.; Kluwer Academic Publishers, Dordrecht, Netherlands, 2003.

36. Huber, Peter J., "Robust Estimation of a Location Parameter," The Annals of Mathematical Statistics, Vol. 35, No. 1, 1964, pp. 73-101.

37. Vanderplaats, Garret N., *Numerical Optimization Techniques for Engineering Design*, 4th ed.; Vanderplaats Research & Development Inc., Colorado Springs, Colorado, 2005.